



This is a repository copy of *Particle-scale observation of seepage flow in granular soils using PIV and CFD*.

White Rose Research Online URL for this paper:

<https://eprints.whiterose.ac.uk/176100/>

Version: Accepted Version

Article:

Sanvitale, N., Zhao, B.D., Bowman, E.T. orcid.org/0000-0001-7868-6688 et al. (1 more author) (2023) Particle-scale observation of seepage flow in granular soils using PIV and CFD. *Géotechnique*, 73 (1). pp. 71-88. ISSN 0016-8505

<https://doi.org/10.1680/jgeot.20.P.432>

© 2021 ICE Publishing. This is an author-produced version of a paper subsequently published in *Géotechnique*. Uploaded in accordance with the publisher's self-archiving policy.

Reuse

Items deposited in White Rose Research Online are protected by copyright, with all rights reserved unless indicated otherwise. They may be downloaded and/or printed for private study, or other acts as permitted by national copyright laws. The publisher or other rights holders may allow further reproduction and re-use of the full text version. This is indicated by the licence information on the White Rose Research Online record for the item.

Takedown

If you consider content in White Rose Research Online to be in breach of UK law, please notify us by emailing eprints@whiterose.ac.uk including the URL of the record and the reason for the withdrawal request.



eprints@whiterose.ac.uk
<https://eprints.whiterose.ac.uk/>

Particle-Scale Observation of Seepage Flow in Granular Soils Using PIV and CFD

N Sanvitale¹, B.D. Zhao², E.T. Bowman¹, C. O'Sullivan³

¹Department of Civil and Structural Engineering, University of Sheffield, Sheffield, UK

²School of Civil Engineering, University College Dublin, Dublin, Ireland (formerly Imperial College London)

³Department of Civil and Environmental Engineering, Imperial College London, London, UK

Abstract

Seepage-induced instabilities pose a challenge in many geotechnical applications. Particle-scale mechanisms govern the initiation of instability. However, current understanding is based on a macro-scale perspective that draws on continuum mechanics. Recent developments in imaging and numerical analysis can provide the particle-scale fundamental perspective needed to develop a comprehensive insight. This contribution demonstrates the value of combining particle-scale experimental and numerical studies. The experiments consider transparent soil samples created using refractive image matching and monitored by particle image velocimetry (PIV). Three-dimensional pore topology is extracted from a series of 2D images and imported into computational fluid dynamics (CFD) simulations. Permeability is estimated by three distinct approaches: using flow rate, PIV- and CFD-generated data. The flow fields obtained from PIV and CFD are in good agreement considering both flow rate contour plots and flow rate distributions; this demonstrates the successful reconstruction of three-dimensional pore structure and flow-field analysis. The comparison also reveals that the side boundary effects in CFD simulations are constrained within a limited region. The multi-plane results characterize the variance of flow

velocity with the three-dimensional pore topology. Finally, the fluid-particle interactions obtained from CFD results show a larger variance in the angular particle packings.

Keywords: Particle-scale behaviour; permeability; seepage; laboratory tests; numerical modelling

Corresponding author: Budi Zhao (budi.zhao@ucd.ie)

1. Introduction

A comprehensive understanding of seepage flow in cohesionless or granular soils is critical in many geotechnical analyses associated with dewatering, dam and flood embankment design, slope stability etc. Seepage analyses to inform engineering design typically adopt a continuum approach with macro-scale parameters. However, the fundamental processes that lead to the internal erosion in embankment dams (ICOLD, 2015) and settlement due to fines migration during dewatering (Preene & Rosser, 2012) initiate at the particle scale. Understanding these processes is important to inform robust approaches to design, e.g. considering whether to continue to use hydraulic gradient rather than seepage velocity when assessing the risk of a seepage-induced instability (Vogt et al., 2015). Incidents such as the failure of Gouhou Dam in 1993 (Zhang & Chen, 2006) and the serious sinkhole incident at WAC Bennett dam in Canada in 1996 (Muir Wood, 2007) remind us of the significant hazard that can be posed by seepage instabilities. Globally, seepage instabilities have caused about 50% of recorded embankment dam failures (Foster et al., 2000). This contribution adopts a combination of particle image velocimetry (PIV) and computational fluid dynamics (CFD) to quantify seepage flow in the void space of a transparent granular soil and to determine the fluid-particle interaction forces that can lead to particle migration and instability.

Saturated transparent soils can be created by refractive index (RI) matching between model (analogue) sands formed of borosilicate glass and carefully selected pore fluids. Illumination by a laser light sheet enables visualization of the particles along a plane within the material, and so the internal mechanisms that underlie complex macro-scale behaviours can be studied (Hunter & Bowman, 2018; Iskander et al., 2015). Hunter and Bowman (2018) developed a transparent soil rigid-walled permeameter to study the particle-scale mechanisms that occur during internal erosion in gap graded particulate systems. They considered a single plane within the sample and successfully imaged particle migration. However, there was no local measurement of fluid flow, and the data generated were two-dimensional. Saleh et al. (1992) and Northrup et al. (1993) applied Particle Imaging Velocimetry (PIV) to tracer particles in the pore fluid to generate 2D images of flow in transparent porous media created using RI matching. Peurrung et al. (1995) applied Particle Tracking Velocimetry using a similar experimental set-up, again obtaining 2D data. Alternatively, the flow fields in 2D transparent micromodels fabricated with soft lithography may be determined with micro-PIV (Karadimitriou et al., 2013; Karadimitriou & Hassanizadeh, 2012; Meinhart et al., 1999). However, it is the 3D geometry of the void space that controls flow in the pores; a complete picture cannot be obtained from planar data. 3D flow data can be obtained using tomographic technologies which can be used on opaque materials, e.g. Magnetic Resonance Imaging MRI and Particle Emission Tomography PET (Khalili et al., 1998; Sederman et al., 1997). However, the data generated are often of limited spatial or temporal resolution.

Computational fluid dynamics (CFD) has been applied to study flow in porous rocks (Mostaghimi et al., 2013; Nunes et al., 2015; Piller et al., 2014) and in sands (Garcia et al., 2009; Taylor et al., 2016, 2017). In these studies, the topology of the pore space was obtained from micro-computed tomography scans. The volumes of soil/rock considered was relatively small, and

ideal flow boundary conditions were typically assumed along the sides of the sample. While the resulting permeabilities appeared reasonable, the accuracy of the velocities within the pores could not be verified, and the implications of the idealized boundary conditions could not be quantified. Huang et al. (2008) and Thaker et al. (2019) determined the 3D topology of the void space in transparent samples, and applied CFD to simulate flow and compared these data with flow field data acquired using PIV. However, the comparisons considered only a single plane and spherical particles.

Developing the work of Hunter & Bowman (2018), this study adopts refractive-index-matched transparent materials and PIV to monitor the flow field in a transparent permeameter. A method was developed to precisely control the laser sheet position in order to enable multiple images of the pore topology and the fluid-flow field to be acquired so that, in contrast to earlier studies, quasi-3D experimental data were recorded. Three-dimensional pore topologies reconstructed from slice-by-slice scanning and image processing are incorporated in CFD simulations. This combination of laboratory experiments and numerical modelling enables the following questions to be addressed:

- i) Can PIV be used to develop a three-dimensional understanding of seepage flow in the void space of granular soils?
- ii) To what extent do the assumed flow boundary conditions compromise the accuracy of the predictions of the local fluid velocities in CFD analyses of seepage flow in the void space of soil?
- iii) Particle migration induced by the fluid-particle interaction force initiates all of the instabilities noted above. Can the combined PIV and CFD analyses enable quantification of the fluid-particle interaction forces in real physical systems?

In a preliminary application of the approach proposed here, we considered two materials with very different particle morphologies and show how this technique can be used to explore the influence of morphology on flow fields and fluid-particle interaction forces.

2. Experimental Setup

2.1. Transparent soil permeameter

The experimental apparatus is a rigid-walled ‘transparent soil’ permeameter that has been designed to visualize the mechanisms occurring during seepage-induced internal erosion in susceptible granular media (Hunter & Bowman, 2018). Fig.1 is a sketch of the experimental device. The permeameter is a rectangular cell (100 mm by 100 mm in plan area and 265 mm high). Five vertical manometer ports are arranged at the back of the permeameter for local head measurements. The flow is directed upward via a constant head applied at the base using an adjustable header tank. Flow from the top of the cell is recirculated back into a reservoir and then pumped back into the header tank. A constant head was applied, and the resulting local head values were measured using the manometers located at the back of the permeameter cell. Consideration was restricted to laminar, low Reynolds number flows, typically encountered in geotechnical applications. Particle movement was not expected since the drag forces were relatively low compared with the particle weights (i.e. gravitational force). Also, analysis of the images showed no visible particle movement throughout testing.

2.2. Laser and imaging systems

A 1.5 mm thick laser sheet parallel to the direction of the flow was applied to the side of the permeameter to illuminate a selected plane perpendicular to the z-axis in Figure 1. The light source was a 1W Kvant continuous wave laser at 520 nm (green) wavelength with variable power control. The laser beam was coupled from the laser head into an optical fibre, recollimated at the fibre output, and then sent through a line generator lens mounted on a lens post and base plate to provide height adjustment. This optical assembly was fixed on a linear micrometre stage with a 25 mm travel range so that specific planes of interest could be imaged and returned to with precision over long-running tests.

A high-speed camera, Phantom Miro 310, mounted on another linear micrometre stage with a 50 mm travel range was positioned in front of the permeameter cell to record images with a spatial resolution of 1280×800 pixels at 200 frames/s. During each test, the position of the camera in the z-direction was adjusted in accordance with the laser sheet position to retain a sharp image focus. A Nikon AF Nikkor lens 85 mm was used with up to 34 mm of extension rings placed between the lens and the camera sensor. All images were recorded using an aperture f -stop number of 4, which was selected according to its influence on the tracer magnification, as discussed later.

2.3. Tested materials

Table 1 shows the physical and optical properties of the two model soils. The first sample consisted of 7.5 ± 0.03 mm diameter spherical beads made of borosilicate glass purchased from SiliBeads. The second sample consisted of angular particles made from Duran® glass with size ranging from 6.7 to 9.5 mm (Sanvitale & Bowman, 2012).

The particle size was chosen based on a trade-off between different aspects related to the optical technique, practical considerations and standard guidelines. As general rule, the size of the particles must be large enough to ensure the tracers can flow easily through the pores without blocking the channels. In addition, the procedure for Standard Test Method for Permeability of Granular Soils (ASTM D 2434-68, 2000) requires the maximum particle size of the specimen to be 8 to 12 times smaller than the diameter of the permeameter. Furthermore, in previous experimental work (Sanvitale & Bowman, 2012) the same refractive index matched material was used and it was observed that the presence of small particles produces a greater amount of scattered light in the granular system owing to the slight differences in refractive indices at the grain–liquid interfaces. It was found that better transparency even at the deepest illuminated sections, can be obtained when large particles are used. Finally, the availability in the laboratory of a sample of angular particles (that are not commercially available but hand-made, see Sanvitale & Bowman 2012) with gradations comparable to those of the beads was taken into account, in order to carry out tests with grains of different shape but compatible drainage behaviour.

Each sample was prepared using a ‘slurry’ placement method to avoid entrapment of air bubbles (Hunter & Bowman, 2018) to create a sample approximately 165 mm in height. In order to develop a uniform pressure and velocity conditions entering the sample, a 45 mm layer of ‘dispersing’ filter material, comprising a mixture of spherical borosilicate beads of 15 mm and 10 mm diameter, was placed at the bottom of the apparatus.

A hydrocarbon immersion fluid (Cargille Laboratories) was chosen to match the refractive index of the glass particles (Sanvitale & Bowman, 2012; Wiederseiner et al., 2011). As well as a close optical match, the fluid and solid mixture needed to behave similarly to soil and water in terms of buoyancy. The effective specific gravity of the particles compared with the fluid was 2.64

– which is typical of soil in water. In order to achieve the best refractive index match during testing, different room temperatures were used, 23 °C for the beads and 26 °C for the angular particles. Figure 2(a) shows a typical outcome of refractive index matching under normal lighting conditions. A small amount of Nile Red fluorescent dye, added to the fluid phase, enabled the application of Planar Laser-Induced Fluorescence (PLIF) based imaging on identifying the solid particles with respect to the fluid phase. To characterize the pore topology, the saturated sample was illuminated by the laser sheet whose wavelength matched the absorption peak of the fluorescent dye within the fluid. The resulting fluorescence (where the dye emits light at a wavelength greater than that of the excitation wavelength) was recorded by the high-speed camera through a long-pass filter placed over the lens to transmit only the fluorescence signal and discard the green laser light: the particles show as dark on a bright fluid background.

3. Particle Image Velocimetry (PIV) Analyses

3.1. Calibration for image size and distortion

Before each test, the image size and distortion were calibrated with fixed grid dots at 1 mm ± 0.001 mm spacing inside the permeameter cell filled with the liquid phase at the locations of the 26 vertical planes imaged in the experiment. The distortion error due to the optical assembly was corrected according to the procedure discussed in Gollin et al. (2017). The coordinates of the dots were estimated with sub-pixel accuracy and associated with an undistorted grid and then interpolated using a built-in MATLAB function Scattered-Interpolant (Brevis et al., 2011). This approach adopts a linear interpolation based on Delaunay triangulation.

3.2. Seed tracers

The fluid flow field was imaged using reflective seed tracers dispersed in the liquid phase. These seeding particles should be neutrally buoyant and small enough to follow the flow accurately. Silver-coated hollow microspheres with a nominal size ranging between 5-30 μm were used at a concentration of 35 mg/l. These had a density of 0.75 g/cm³, resulting in an effective specific gravity of 1.13 compared to the fluid, i.e. close to unity. To ensure that the inertia effects due to particle density were negligible so that the tracers would reliably follow the flow, the Stokes number was calculated as follows:

$$Stk_s = \frac{\rho_s d_s^2 u_y}{18 \nu \rho D} \ll 1 \quad (\text{Eq. 1})$$

where d_s and ρ_s are the seed diameter and density, respectively, D the bead diameter, ν and ρ the fluid kinematic viscosity and density, respectively, and u_y is the axial (y-direction) fluid velocity of the flow. For our set-up, the maximum Stokes number was calculated to be $Stk_s = 2.59 \times 10^{-6}$. The movement of the tracers was recorded by removing the long-pass filter in front of the camera lens to allow the light reflected from their surfaces to be captured. Figure 2(b) and (c) show how laser illumination enables internal visualization of a plane within both spherical bead and angular particle samples with the tracers. Two videos, V1 and V2 in the supplementary material, show the movement of tracers in both spherical bead and angular particle samples. Figure 2(d) shows the top view of the laser sheet illuminated plane with a finite thickness of around 1.5 mm.

3.3. Image acquisition for 3D volumes

The flow fields inside two 3D volumes were examined within each sample. The lower volumes were located between manometer ports P2 and P3 and denoted as sub-volumes Beads-L and Ang-

L for the spherical sample and angular samples, respectively (Figure 1). The upper volumes were located between manometer ports P3 and P4 and denoted as sub-volumes Beads-U and Ang-U, respectively. The dimensions of sub-volumes varied slightly with the position of the high-speed camera, as shown in Table 2. In each sub-volume, the flow fields on 26 planes parallel to the flow directions were measured. These planes were evenly spaced at $1\text{ mm} \pm 0.001\text{ mm}$, centred in the mid-section of the permeameter cell with at least 32 mm distance from the lateral sidewalls. The choice of inter-plane spacing was made based on the laser sheet thickness of 1.5 mm. On each plane, a series of images were taken over 2 seconds at 200 frames/s, i.e. 400 images were taken per plane.

3.4. PIV postprocessing

An open-source software, PIVlab (Thielicke & Stamhuis, 2014), was used for image processing to determine the flow velocities. PIVlab gives an Eulerian description of the investigated velocity field, estimating the displacement for groups of tracers by determining the peak of the cross-correlation of many small interrogation areas. This software uses a multi-pass cross-correlation algorithm coupled with a window deformation technique to obtain the velocity vectors (Thielicke, 2014). The 2-step correlation algorithm with decreasing window size (D_I) was used to evaluate the recorded images with a final size of 32×32 pixels (approximately $1 \times 1\text{ mm}^2$ area), set to minimize the loss of in-plane particle pairs ensuring that the x and y displacements were smaller than $D_I/4$. The loss of particle pairs between corresponding interrogation windows due to out-of-plane motion was limited due to the fact that the z displacement of the tracer particles, which can be assumed to be of the same magnitude as the tracer particle displacement in the x-

direction, was less than a quarter of the light sheet thickness (Atkins, 2016; Keane & Adrian, 1993).
The overlap of the interrogation windows was 50% for all steps.

The velocity fields for each plane position were calculated by averaging over 2 s of recorded images, and the ‘instantaneous velocities’ were estimated on two successive frames separated by a time steps Δt . The frame rate was 200 fps for all of the experiments. The influence of the time step on the fluid velocities was studied by setting Δt equal to 5, 10, 20 and 40 ms, equivalent to 1, 2, 4 and 8 frames (Figure S1 is provided as supplemental material). Decreasing Δt from 40 to 10 ms caused an increase in the time-averaged u_y and u_x values. Further decreasing Δt from 10 to 5 ms led to little variation in either u_y or u_x , meaning the true maxima of velocity were captured at a time step of around 10 ms. Therefore, a time step Δt of 10 ms was chosen for the PIV analyses to avoid positional errors associated with reducing the time step to very low values (Gollin et al., 2017).

The seeding density was approximately five tracers inside an interrogation window for both tests (as shown in Figure S2 in the supplemental material) which is within the optimal range to achieve a successful correlation and minimum random error (Thielicke, 2014). The seed image size d_τ was estimated as the width of the autocorrelation peak of a typical set of interrogation windows (Michaelis et al., 2016; Patil & Liburdy, 2013). The autocorrelation peak width was calculated using the e^{-2} width. The resulting widths were 3.57 ± 0.72 pixels for the test with the spherical beads and 3.27 ± 0.81 pixels for the test with angular particles (Figure S3). Both sizes lie in the range of the tracer image diameter to achieve optimal measurements using the window deformation algorithms in PIVlab (Thielicke, 2014).

3.5. Boundary flow field on a single plane

Figure 3 shows a typical flow field across the whole permeameter for a sample of beads, considering three sub-volumes in the left, middle and right, respectively. The PIV analyses performed here show how the rigid lateral boundaries of the permeameter can disrupt the particle packing, leading to some areas of large flow velocity in comparison to the mean, for example with the high flow at the left boundary of Figure 3(a) compared to (b) and (c). In this preliminary examination of the flow, an image mask was manually applied to the particle positions to exclude them from the fluid flow analysis. In contrast, for the following analyses focused on volumes at the centre of the permeameter, the masks were automatically determined from image processing.

4. Image Processing

4.1. Image segmentation

Figure 4(a) shows a typical grey-scale image of a plane from sample Beads-U, illuminated by the laser. As shown in the schematic diagram at the top of the image, the finite laser thickness leads to non-uniform grey values because particles can partially fill the laser beam. This is similar to the partial volume effect associated with microCT images and consequences for image quality are related to the laser thickness. The histogram of grey values of the image as shown in Figure 4(b) indicates there is no clear separation between the grey values for the particles and the pore-space. The distance between the scanning planes determines the image resolution in the z-direction, i.e. the effective voxel length in the z-direction is 1 mm. Furthermore, the laser sheet creates linear streaks or shadows in the direction of the laser, with grey values that can be similar to that of particles. In previous studies, the 3D pore space was reconstructed by identifying the centre and

radius of each spherical particle from 2D slices (Huang et al., 2008; Thaker et al., 2019) rather than considering the 3D dataset directly. This shape-matching approach cannot be used for samples with irregular-shaped particles.

Image segmentation of granular materials classifies each pixel as being either within a particle or within the pore-space. We explored three approaches to segment the images, and Figure 5 presents the results of each of these methods applied to three representative slices. The first approach is threshold segmentation which classifies all pixels with a grey value lower than a specified threshold as being in the particle phase and the remaining in the pore phase. The threshold can be automatically determined by Otsu's algorithm based on the grey value histogram, as shown in Figure 4(b) (Otsu, 1979). The Otsu-threshold segmentation method incorrectly classified some linear shadows created by the laser as being in the particle phase.

The other two methods considered, namely the trainable Weka (Waikato Environment for Knowledge Analysis, Arganda-Carreras et al., 2017) and the U-Net (Ronneberger et al., 2015), are based on artificial intelligence. Artificial intelligence segmentation approaches learn from manually segmented images to define a pixel-wise classifier which labels each pixel as being in either the particle or pore phase. The trainable Weka algorithm was developed in the open-source software platform Fiji (Schindelin et al., 2012). When compared with the Otsu threshold, this method improved the segmentation quality to some extent, but it could not completely remove the laser-induced linear shadows. Finally, the U-Net algorithm proved to be more robust in segmentation, producing smooth particle-pore interfaces and no linear shadows, in contrast with the other two methods. The segmented results from U-Net have smooth particle surfaces, no internal voids in the particles and eliminate all linear artefacts induced by the laser, which is important for constructing CFD models. U-Net performs segmentation based on both grey values

and morphological patterns, e.g., edges, curvatures, and spheres. The U-Net package was implemented in Tensorflow and Keras following the U-Net architecture proposed by Ronneberger et al. (2015).

The U-Net segmentation procedure can be divided into three major steps: (a) data preparation for training; (b) U-Net training; and (c) new image segmentation (Figure 6). The U-Net architecture requires an image dimension of 512×512 . Therefore, the images were scaled from 1280×800 pixels to 512×512 pixels and scaled back after segmentation. Initially, eight images were segmented by visual inspection. Data augmentation was performed to increase the diversity of training data by shifting and rotating each annotated image to produce four images. Thus a total of 32 images were obtained for training and validation. Then the U-Net algorithm was trained with 32 annotated images to define the classifier. The trained U-Net classification led to an accuracy of about 93% for validation images and was used as a classifier to segment new images. The U-Net classification generated a grey-scale image in which the grey value of a pixel reflected the possibility of that pixel being in a particle. A target porosity was specified to generate an appropriate threshold grey-level value to binarize the output of the U-Net algorithm. This porosity was selected by considering the experimental whole-sample value. However, acknowledging the sample heterogeneity, a parametric study was carried out considering a range of reasonable local porosity values as discussed below.

4.2. Three-dimensional pore structure reconstruction

The slice-by-slice scanning method led to an in-plane pixel size of approximately 0.029 mm along the x- and y-axes, and an out-of-plane distance of 1 mm along the z-axis. Therefore, we applied a scaling to the output from U-Net to reconstruct a three-dimensional volume with an

identical voxel size of 0.1 mm along all directions. Figure 7 shows the effect of upscaling along the z -direction with three different interpolation methods. The scaling without interpolation results in a stepped particle surface, while both interpolation methods provide relatively smooth particle surfaces. The bilinear interpolation is adopted in this study. Finally, we binarized the scaled three-dimensional images with a threshold value to reach the porosity value determined experimentally. The threshold value was determined from the linear relationship between the threshold value and the resulting porosity. Three levels of porosity were used to reconstruct the pore topology to investigate the influence of porosity on the CFD results.

We performed marker-based watershed labelling to identify individual particles from three-dimensional binary images. The image processing steps involved in labelling particles are: (a) construct a distance map representing the distance from a pixel to its closest particle surface; (b) use marker identification based on the H-Maximum algorithm (Soille, 2013) on the distance map; (c) implement marker-based watershed segmentation using the markers and distance map. A more detailed description of this marker-based watershed segmentation approach can be found in Zhao et al. (2015). Figure 8 illustrates the labelling results on typical 2D slices for beads and angular particles. The particles are less regular on x - z planes than on x - y planes. This is mainly due to the finite step distance during the slice-by-slice scanning along the z -axis.

A marching cubes algorithm was used to generate triangular surface meshes from the voxel assembly representing individual particles (Lorensen & Cline, 1987). The surface meshes of individual particles were cleaned, simplified and smoothed with GMSH, an open-source mesh generator (Geuzaine & Remacle, 2009). Finally, the surface meshes of all particles were combined into a single file with individual particles represented by a unique label. Figure 9(a) and (b) show

the three-dimensional views of the particle packings in the scanning region for the samples with spherical beads and angular particles, respectively.

5. Computed Fluid Dynamics (CFD) Simulation

5.1. Governing equation and numerical method

For the fully saturated conditions assumed here, flow through the pore space is governed by the incompressible Navier-Stokes equations formulated as:

$$\rho_f \left(\frac{\partial \mathbf{u}}{\partial t} + \mathbf{u} \cdot \nabla \mathbf{u} \right) = -\nabla p + \mu \nabla^2 \mathbf{u} \quad (\text{Eq. 1})$$

$$\nabla \cdot \mathbf{u} = 0 \quad (\text{Eq. 2})$$

where \mathbf{u} is the velocity vector, and p is the pressure. In the steady-state, $\partial \mathbf{u} / \partial t = 0$. Here the Navier-Stokes equations were solved using the Semi-Implicit Method of Pressure Linked Equations (SIMPLE) algorithm in the open-source CFD toolbox OpenFOAM (OpenFOAM Foundation, 2019). The SIMPLE algorithm is a steady-state solver for incompressible flow. The CFD analysis provides the velocity and pressure values at the centre of each CFD cell.

The simulation domain was discretized by the mesh generation algorithms available in OpenFOAM, i.e., BlockMesh and SnappyHexMesh. BlockMesh decomposes the simulation domain into blocks, while SnappyHexMesh takes the surface mesh defining the pore structure and chisels it with the geometry defined by the combined surface mesh file. We applied localized refinement at the particle surface, which increased the mesh densities close to the particle-particle contacts in particular. This created CFD meshes with around 3.5 million cells. Figure 9(c) and (d) show typical CFD meshes of pore space for spherical beads and angular particles, respectively.

In all simulations, a constant pressure boundary condition was applied at both the inlet (17 Pa) and outlet boundaries (0 Pa). A ‘slip’ condition was applied to the four lateral boundaries so that the velocity component normal to each of these boundaries was set to be zero while the tangential velocities remained unconstrained. A ‘no-slip’ boundary condition was applied to the particle surfaces so that the velocities normal and tangential to the surface were set to zero. These boundary conditions are similar to those applied in the CFD analyses by Taylor et al. (2016). They do not capture the heterogeneity of the pressure and velocity distributions that exist on the boundaries of sub-volumes in experiments. However, the flow velocity data available from the experiments are restricted to 2D and limited to 26 discrete vertical planes. A valid CFD analysis requires conservation of mass (adherence to continuity) in the model in all three dimensions. Consequently, it was not possible to use the experimental data to apply non-uniform velocity fields along the boundary to the simulation domain.

The normal and shear stresses on the particle surface were determined from the flow velocity and pressure fields. Each particle surface was discretized into surface elements. Then, the flow-induced force and moment on individual particles were calculated by integrating normal pressure and viscous shear stresses over all elements on the particle surface:

$$\mathbf{F}_p = \sum_{i=1}^{N_e} \rho p_i A_i \mathbf{n}_i \quad (\text{Eq. 3})$$

$$\mathbf{F}_v = \sum_{i=1}^{N_e} \mu \mathbf{R}_{dev} A_i \quad (\text{Eq. 4})$$

where N_e is the number of elements covering the particle surface, ρ is the fluid density, p_i is the kinematic normal pressure, A_i and \mathbf{n}_i are the patch area and normal vector, μ is the fluid dynamic

viscosity, and \mathbf{R}_{dev} is the deviatoric stress tensor. The integration was performed using the in-built function, ‘forces’, in OpenFOAM (OpenFOAM Foundation, 2019).

5.2. Validation with regular packings

The CFD simulation data are inherently dependant on the mesh density (cell size) (e.g. Knight et al. 2020). The sensitivity of the fluid-particle interaction forces obtained from the CFD modelling approach adopted here to the mesh density was examined by considering the data in Zick & Homsy (1982) for simple cubic (SC) and face-centred cubic (FCC) packings of uniformly sized spheres. Following Knight et al (2020), the models exploited geometric symmetry to reduce the calculation cost. As before, a specified pressure was applied at the inlet and outlet, while ‘cyclic’ boundary conditions were applied to the four lateral boundaries. The sphere centroids were placed on a fixed lattice, and the particle sizes were changed to reach different packing densities; e.g. the particle diameter was increased from 4.4 mm to 4.9 mm in the FCC packings to achieve porosity between 0.495 and 0.303. The fluid-particle interaction coefficient, $\bar{F}_{f \rightarrow s}$, is the fluid-particle interaction force normalized by Stokes drag force $F_{f \rightarrow s}^S$:

$$F_{f \rightarrow s}^S = 3\pi\mu D|u| \quad (\text{Eq. 5})$$

$$\bar{F}_{f \rightarrow s} = F_{f \rightarrow s} / F_{f \rightarrow s}^S \quad (\text{Eq. 6})$$

where D is the particle diameter, u is the superficial flow velocity, and $F_{f \rightarrow s}$ is the fluid-particle interaction force, which includes both the pressure and viscous terms.

The fluid-particle interaction coefficient increases with reduced packing porosity, as shown in Figure 10(a). The results from CFD simulations are consistent with the Zick and Homsy solutions and the results from Immersed Boundary Method (IBM) obtained by Knight et al. (2020). The

CFD results are mesh dependent. As shown in Figure 10(b) and (c), the agreement between the fluid-particle interactions obtained from these CFD simulations and the Zick and Homsy data, $|\bar{F}_{f \rightarrow s} - \bar{F}_{f \rightarrow s}^{ZH}|/\bar{F}_{f \rightarrow s}^{ZH}$, improves with increasing mesh density, D/d_m , where D is the particle diameter, and d_m is a characteristic mesh element size. At the same D/d_m , the relative error increases with sample density. The relative errors for most samples were smaller than 5% at a D/d_m of 40. The results obtained from the unstructured mesh CFD analyses by Knight et al. (2020) show a similar influence of mesh density on relative error for drag estimation. The average ratio between particle diameter and mesh element size was chosen to be 40 for the permeameter simulations.

6. Results

The 2D-PIV measurements can only provide the components of flow velocities in the plane of the laser, i.e. along the x- and y-directions. Within this plane, the distance between PIV data points is around 0.5 mm, which is much larger than the CFD mesh size. Therefore, the CFD velocity fields were interpolated to the centre of the PIV interrogation regions to allow a direct comparison between the PIV and CFD results. The Reynolds number in this study is around one, which indicates a laminar flow condition. We normalized the velocity values by the mean vertical velocity either on each vertical slice (\bar{u}^s) or the mean value in each sub-volume (\bar{u}^v).

For each sub-volume, the PIV analysis was performed on 26 x-y planes at 1 mm intervals. The x-y planes were referred with their z coordinates from 0 mm to 25 mm. The CFD domain is slightly smaller than the PIV domain and has 24 x-y planes ($z = 1$ to 24 mm) to reduce the effects of upscaling on boundary slices (Figure 7). The sub-volume has about six particles along the x-direction and four particles along the y-direction, and there are about 20 particles completely inside each sub-volume.

6.1. Permeability estimation

Table 3 shows the experimental measurements for each sub-volume. Each sub-volume is named by the particle type, e.g. spherical (Beads) and angular (Ang), followed by the position, e.g. upper (U) and lower (L). The overall packing porosity, n , permeameter cross-section area, A_{Exp} , and flow rate, Q_{Exp} , were measured during each permeameter test. Local manometer readings were used to identify the hydraulic gradient for the experiments, and the two sub-volumes in the angular particle sample had slightly different hydraulic gradients i_{exp} due to the inhomogeneous packing. Seepage flow rates were determined from experimental measurements (u_{seep}^{Exp}), PIV analysis (u_{seep}^{PIV}) and CFD simulations (u_{seep}^{CFD}).

Figure 11 compares the permeability values estimated by the three types of seepage velocities. In general, the permeability values estimated by PIV analysis (k^{PIV}) are smaller than the values estimated from the experimental measurements (k^{Exp}). This is unsurprising as the PIV analysis was performed over central sub-volumes, while the pump injection rate measures the cross-section of the permeameter, including the larger voids commonly encountered at the side walls (Figure 3). In addition, the sub-volumes for Ang show smaller permeabilities than the sub-volumes for Beads. For k^{Exp} the sub-volume Ang-U has a higher permeability than for Ang-L due to the different hydraulic gradient as measured using the manometers, while there was no evident difference in the sub-volumes of the Beads sample. In Figure 11(a) the k^{CFD} data were obtained using the overall experimental porosities, i.e. $n=0.38$ and 0.36 in the CFD simulations for Beads and Ang samples, respectively. Perhaps surprisingly, the permeability values estimated by CFD simulations, k^{CFD} (grey data points), are similar across the four sub-volumes, with only a slight decrease for the Ang sample compared to the Beads. This means that, while the permeabilities estimated for CFD and

PIV in the Beads sub-volumes are quite close, for the angular sample, k^{CFD} measurements are approximately twice that of k^{PIV} .

The differences between experimental and numerical permeabilities could be caused by (a) local porosity variations, (b) CFD boundary effects, or (c) PIV velocity measurement errors. Figure 11(b) illustrates the sensitivity of the k^{CFD} results to porosity by considering three limiting plausible porosity values. For Beads-U, k^{CFD} agrees with both k^{Exp} and k^{PIV} if local porosity is changed from 0.38 to 0.40. For Ang-U, k^{CFD} agrees with k^{Exp} and k^{PIV} if the local porosity is changed from 0.36 to 0.31 and 0.29, respectively. However, the segmented images seem to be inconsistent with the grey-value images due to the large porosity change (Figure S4 in the supplementary material). Furthermore, the variation in porosity had only a limited influence on the flow field distributions. Potential PIV velocity measurement errors were also investigated by changing the framerate. However, this did not lead to a noticeable change. A definitive, precise explanation for the inconsistency in the permeability values could not be determined.

6.2. Flow fields – contour plots

The normalized flow fields obtained from PIV and CFD analysis within a typical x-y plane for the Beads-U sub-volume are in good agreement, as shown by the normalized horizontal velocity \bar{u}_x^s and vertical velocity \bar{u}_y^s in Figure 12. The heterogeneity in the packing leads to concentrated flow paths for vertical flow at some large voids, e.g. close to the left bottom corner. The horizontal velocity is determined by the local pore alignment relative to the macro-scale flow direction. The lateral boundaries assumed in the CFD models prohibit horizontal flow, so the flow patterns at the side boundaries differ. For example, the physical test data indicate a relatively large horizontal flow close the left boundary in Figure 12(a) which is not captured in the CFD model in Figure

12(b). The difference in the boundary conditions also influences the vertical velocity values in this region. The vector plots of flow fields on three x-y planes are shown in Figure 13 to further demonstrate the similar patterns revealed by PIV and CFD estimations. Again, the lateral boundary conditions inhibit horizontal flow in the CFD model.

The flow velocities on four x-y planes in the Beads-U sub-volume were analysed statistically, as shown in Figure 14. The horizontal normalised velocity \bar{u}_x^s tends to form a Laplace distribution with a mean velocity around zero (Figure 14(a)). While the distributions obtained from the PIV analyses are similar for the four planes considered, the two CFD distributions with $z = 1$ mm and 24 mm tend to have a higher proportion of data points with a velocity close to zero, due to the lateral boundary effect experienced at the front ($z = 1$ mm) and back ($z = 24$ mm) of the studied volume. The vertical normalised velocity \bar{u}_y^s tends to form a half Laplace distribution (Figure 14(b)). Similarly, the planes close to the front or back lateral boundary in the CFD simulation ($z = 1$ mm and 24 mm) have a higher proportion of velocity close to zero. The cumulative distributions in Figure 14(c) and (d) show a good agreement between PIV and CFD results.

The pore topology is intrinsically correlated with particle morphology and granular material packing/fabric. The flow fields on three x-y planes of the Ang-L sub-volume show the flow patterns that are distinct from those developed in the Beads-U sub-volume (comparison between Figure 15 and Figure 13). Some flow channels are straight rather than converging-diverging due to the flat surfaces of angular particles, as indicated by arrows. The difference seems to be more obvious for the angular particle sample than for the beads sample. However, the overall distribution of flow velocity in the angular particles sample is very similar to that of the beads sample, as shown in Figure 16. Previous studies have indicated that the flow velocity distribution

depends on packing density (Rong et al., 2013). Further tests are needed to investigate the influence of particle shape on the flow velocity distribution.

The mapping of the CFD data onto the PIV grid allows spatial variation of the difference between the two datasets to be examined, as shown in Figure 17(a) and (b). While the data in Figure 12 showed the similarity of the flow patterns, there are large differences between the normalized velocity intensities. Figure 17(c) and (d) show the cumulative distributions of the velocity difference values for five x-y planes. The difference mainly lies between $\pm 50\%$ and $\pm 100\%$ of the mean seepage velocity on each slice for horizontal and vertical velocity, respectively. Perhaps unsurprisingly, the planes closest to the lateral boundaries ($z = 1$ or 24 mm) have a higher velocity difference.

6.3. Mean flow rate on slices

Here, the mean velocity on each x-y plane is normalized by the seepage velocity in each sub-volume. The normalized vertical velocity on each plane varies between 0.5 and 1.5, as shown by Figure 18(a). The PIV and CFD data exhibit similar patterns of variation in $\langle \bar{u}_y^v \rangle$ along the z-axis. In the CFD analyses, the lateral boundaries prohibit out-of-plane flow and lead to low velocity values along z, as shown by the shaded area in Figure 18(b). However, $\langle \bar{u}_z^v \rangle$ increases to the expected level after about 3 mm ($\sim D/2$) from the lateral boundary. The heterogeneity of the pore structure and relatively small sub-volume leads to a large variance of the plane-based porosity (Figure 18(c)). For example, the plane-based porosity for the Beads-U sub-volume ($n = 0.38$) varies from 0.25 to 0.5.

The CFD analyses provide 3D data, enabling analysis of the velocity distribution in horizontal x-z planes perpendicular to the flow direction. As expected, the variance of the mean vertical

velocity $\langle \bar{u}_y^v \rangle$ on x-z planes is inversely correlated to the plane porosity due to the fluid continuity (Figure 19(a) and (b)). Where the porosity in the x-z plane is lower, $\langle \bar{u}_y^v \rangle$ is higher so that overall flow rate is the same for each x-z plane in line with the principle of mass conservation. The pressure dissipation is higher at the lower porosity plane, as shown in Figure 19(c).

6.4. Fluid-particle interactions

Each sub-volume contains around twenty particles that do not intersect the boundaries. Figure 20 shows the vector plots of the fluid-particle interaction coefficients $\bar{F}_{f \rightarrow s}$ (Equation 6) projected onto x-y planes for four sub-volumes. The magnitudes of $\bar{F}_{f \rightarrow s}$ have a large variance, especially for angular particles. The directions of $\bar{F}_{f \rightarrow s}$ slightly deviate from the flow direction – the mean deviation angle equals 16° . The variance of $\bar{F}_{f \rightarrow s}$ arises mainly from the heterogeneous flow fields, resulting from local packing and irregular particle morphologies.

Figure 21(a) shows the distribution of the fluid-particle interaction coefficient, which varies approximately from 50 to 140 for beads and from 50 to 240 for angular particles. The mean value of $\bar{F}_{f \rightarrow s}$ is influenced by the different packing densities, with the angular particle sample having a slightly higher packing density than the beads sample. Figure 21(b) shows the fluid-particle interaction coefficients normalized by their mean values. Clearly, the sample with angular particles has a higher variance than the spherical beads sample. This variance may arise from packing density or particle shape difference.

The fluid-particle interaction is contributed by two components, i.e. a viscous component due to skin friction and a pressure component due to the pressure gradient. In dense packings, the pressure component of fluid-particle interactions dominates the fluid-particle interaction, while the viscous component accounts for about 20% on average, as shown in Figure 22(a). Spherical beads

tend to experience a slightly higher ratio of the viscous component to pressure component than angular particles. Figure 22(b) shows the deviation angle of fluid-particle interactions from the flow direction, i.e. $\theta_d = \arctan(\bar{F}_{f \rightarrow s, xz} / \bar{F}_{f \rightarrow s, y})$. Most particles have a deviation angle between 0° and 30° .

7. Conclusions

This study investigated pore-scale seepage in granular packings with the combined experimental and numerical methods. Permeameter tests were performed with transparent soils consisting of spherical and angular particles. PIV analysis quantified 2D flow fields inside granular packings on multiple planes. We adopted a series of image processing techniques to reconstruct the 3D pore topologies from the slice-by-slice scanning images. Pore-scale CFD analysis was performed on reconstructed volumes to obtain both flow fields and fluid-particle interactions. The fluid-particle interactions obtained by CFD simulations were validated with existing results on regular particle packings. The conclusions are summarised as follows.

PIV analysis can quantify the flow field for two-dimensional planes. The random packing of particles leads to preferential flow paths at larger voids (e.g. close to boundary wall). Spherical particles tend to form converging and diverging flow paths, while angular particles with flat surfaces form straight channels. The interplays between local particle arrangement, particle shape and pressure gradient determine the heterogeneous pore-scale flow fields.

The slice-by-slice images containing pore structure information were obtained by illuminating the transparent soils at multiple locations with a sheet laser. An artificial intelligence algorithm provided good image segmentation results for the images with poor contrast and artefacts. The flow fields obtained from CFD analysis on the reconstructed pore structure show a good agreement

with PIV results. Similar patterns were obtained for the contour plots of flow fields, flow vector plots and velocity magnitude histograms. This agreement demonstrates the successful implementation of the three-dimensional pore structure reconstruction methods. However, while there is good agreement between the average flow fields, the local differences in flow field data are more significant.

This work supports the development of systems with thinner lasers (including the requisite safety considerations) and exploiting recent advances in automated systems for macro photography to reduce the observed partial volume effects and improve the resolution orthogonal to the scanning planes (i.e. in the z-direction considered here).

The CFD results have a higher resolution in comparison with the PIV results and produce three-dimensional velocity values. However, the analyses tend to have side boundary effects. The comparison between CFD and PIV results indicate the side boundary effects are usually constrained within a half particle diameter region. The point-by-point comparison of CFD and PIV results was performed after downscaling the CFD results. The normalized velocity difference remains large, even though the overall distribution of CFD and PIV flow fields are similar.

The fluid-particle interactions obtained from fully resolved CFD analysis are consistent with previous numerical solutions. The fluid-particle interactions obtained the permeameter model tests have a large variance, especially for angular particles. For relatively dense packings, viscous drag contributes to a small fraction of the total fluid-particle interaction. The fluid-particle interaction slightly deviates from the injection direction. However, for this study, the number of particles in each CFD model was relatively small (around twenty), and the beads and angular particles samples have slightly different packing density. Therefore, the fluid-particle interaction results should be further investigated to elaborate on the particle shape effects.

List of Figure and Table Captions

Figure 1. Schematic of the experimental set up.

Figure 2. Images of experimental setup: (a) Permeameter cell partially filled with oil; (b) Beads sample illuminated by laser sheet; (c) Angular particles sample illuminated by laser sheet; (d) top view of the laser sheet.

Figure 3. Flow fields in the (a) left, (b) middle and (c) right for the permeameter with beads.

Figure 4. (a) Typical grey-scale image in Beads-U sub-volume, $z = 0$ mm. (b) Histogram of grey values. Inset in (a) shows that the non-uniform intensity is a consequence of the finite laser width.

Figure 5. Segmentation results for three typical slices in Beads-U sub-volume using three different segmentation methods: threshold segmentation with Otsu's threshold, trainable Weka segmentation, and U-Net segmentation. Note: red-dashed circles indicate the artifacts produced by inaccurate segmentation.

Figure 6. U-Net segmentation procedure for Beads-U sub-volume: (a) Step-1: prepare training and validating data sets; (b) Step-2: train U-Net algorithm; (c) Step-3: apply trained U-Net as a classifier for segmenting new images.

Figure 7. Upscaling along z -direction on the U-Net classified image for Beads-U sub-volume: (a) Unscaled image data; (b) Image obtained by scaling without interpolation; (c) Image obtained by scaling with bilinear interpolation; (d) Image obtained by scaling with bicubic interpolation.

Figure 8. Labelled images with particles represented by different colours for Beads-U sub-volume on (a) x - y plane and (b) x - z plane and Ang-U sub-volume on (c) x - y plane and (d) x - z plane.

Figure 9. Three-dimensional views of the combined surface meshes for (a) Beads-U sub-volume and (b) Ang-U sub-volume. Note: colour is used to distinguish the surfaces of individual

particles. Hexahedron meshes which discretize pore structure for CFD simulation for (c) Beads-U sub-volume and (d) Ang-U sub-volume.

Figure 10. Verification of CFD modelling approach: (a) Confirmation of ability to capture the influence of porosity on the fluid-particle interaction coefficient $\bar{F}_{f \rightarrow s}$, dashed lines indicate a curve fit to the Zick & Homsy (1982) data; (b) Mesh dependence of $\bar{F}_{f \rightarrow s}$ for SC packings; (c) Mesh dependence of $\bar{F}_{f \rightarrow s}$ for FCC packings. The results predicted by the Immersed Boundary Method (IBM) with a regular grid and from fully resolved CFD using an unstructured meshes from Knight et al. (2020) are included in (a) and (c), respectively.

Figure 11. (a) Hydraulic permeability values predicted by experiments, PIV and CFD measurements. (b) Influence of porosity on hydraulic permeability as estimated by CFD modelling for Beads-U and Ang-U sub-volumes. The prediction results from Kozeny-Carman Equation (KC Eq.) is included in (b).

Figure 12. Comparison of the PIV and CFD flow fields in Beads-U sub-volume on the vertical slice with $z = 16$ mm.

Figure 13. Comparison of the PIV and CFD flow fields in Beads-U sub-volume on three slices with $z = 1, 8$ and 16 mm. Velocity vector length is normalized by seepage velocity.

Figure 14. Cumulative distributions of flow velocity at four vertical planes in Beads-U sub-volume obtained from PIV and CFD results.

Figure 15. Comparison of the PIV and CFD flow fields in Ang-L sub-volume on three slices with $z = 1, 8$ and 16 mm. Velocity vector length is normalized by seepage velocity. Arrows indicate narrow flow paths.

Figure 16. Cumulative distributions of flow velocity at four vertical planes in Ang-L sub-volume obtained from PIV and CFD results.

607 Figure 17. Difference between PIV and CFD flow fields for the vertical slice with $z = 16$ mm in
608 Beads-U sub-volume: (a) horizontal velocity; (b) vertical velocity. The cumulative
609 distributions of PIV and CFD difference for (c) horizontal velocity and (d) vertical velocity on
610 five typical slices in Beads-U sub-volume.

611 Figure 18. Variation of the mean velocity values obtained from PIV and CFD results and the slice
612 porosity on x-y planes parallel to flow direction.

613 Figure 19. Variation of mean vertical velocity, porosity and hydraulic gradient on x-z planes
614 perpendicular to flow direction predicted by CFD simulations.

615 Figure 20. Projection views of drag force vectors for the particles that are not intersecting with
616 boundary walls.

617 Figure 21. Cumulative distributions of (a) fluid-particle interaction coefficients for beads and
618 angular particles and (b) the normalized fluid-particle interaction coefficients.

619 Figure 22. Distributions of (a) the ratio between pressure and viscous drag components, and (b)
620 the angle between fluid-particle interaction and flow direction.

621 Table 1. Particle and fluid properties

622 Table 2. Sub-volume dimensions

623 Table 3. Experimental and numerical measurements for each sub-volume

624 Figure S1. Example of the effect of time resolution of PIV analysis on the estimate of the time
625 averaged component (a) u_x and (b) u_y . The velocities are estimated along the yellow dashed
626 lined shown in the inset of (a).

627 Figure S2. Distribution of the number of tracers for a subsets of interrogation windows (32 x 32
628 pixels) for (a) beads and (b) angular particles.

629 Figure S3. Autocorrelation function for a subsets of interrogation windows (32 x 32 pixels) for (a)
630 beads and (b) angular particles. Histogram of autocorrelation peak width for (c) beads and (d)
631 angular particles.

632 V1. Video of an illuminated section in the bead sample showing the movement of tracers

633 V2. Video of an illuminated section in the angular sample showing the movement of tracers

634

Nomenclature

A_{Exp}	permeameter cross section area
A_i	area of CFD mesh element
d_m	characteristic mesh size
d_s	seed particle diameter
D	diameter of beads and angular particles
D_I	interrogation window size
$F_{f \rightarrow s}^S$	stokes drag force
$\bar{F}_{f \rightarrow s}$	fluid-particle interaction coefficient
$\bar{F}_{f \rightarrow s, xz}$	projection of fluid-particle interaction coefficient on x-z plane
$\bar{F}_{f \rightarrow s, y}$	projection of fluid-particle interaction coefficient on flow direction – y axis
$\bar{F}_{f \rightarrow s}^{ZH}$	fluid-particle interaction coefficient from Zick and Homsy solutions
F_p	pressure component of fluid-particle interaction force
F_v	viscous component of fluid-particle interaction force
k^{CFD}	hydraulic permeability determined through CFD analysis
k^{Exp}	hydraulic permeability determined through experimental measurements
k^{PIV}	hydraulic permeability determined through PIV analysis
n	packing porosity
n_i	normal vector of CFD mesh element
N_e	number of CFD mesh element on particle surface
p	fluid pressure
p_i	kinematic normal pressure on CFD mesh element

Q_{Exp}	permeameter flow rate
R_{dev}	deviatoric stress tensor
Stk_s	Stokes number for seed particles
Δt	time step used for PIV analysis
\mathbf{u}	fluid velocity vector
u_x	component of fluid velocity in the x -direction
u_y	component of fluid velocity in the y -direction
u_z	component of fluid velocity in the z -direction
u^s	velocity magnitude normalized by mean seepage velocity on each slice
u^v	velocity magnitude normalized by mean seepage velocity in each sub-volume
$\langle u^v \rangle$	mean velocity on slice normalized by mean seepage velocity in each sub-volume
u_{seep}^{Exp}	seepage velocity determined through experimental measurements
u_{seep}^{PIV}	seepage velocity determined through PIV analysis
u_{seep}^{CFD}	seepage velocity determined through CFD simulations
v_{seep}	seepage flow velocity
μ	fluid dynamic viscosity
ρ	fluid density
ρ_s	seed particle density
ν	fluid kinematic viscosity
θ_d	deviation angle of fluid-particle interaction from the fluid injection direction

635

636 **Acknowledgments**

637 This research was funded by EPSRC grant EP/P010393/1 and EP/P010423/1.

References

- Arganda-Carreras, I., Kaynig, V., Rueden, C., Eliceiri, K. W., Schindelin, J., Cardona, A., & Sebastian Seung, H. (2017). Trainable Weka Segmentation: A machine learning tool for microscopy pixel classification. *Bioinformatics*, 33(15), 2424–2426.
- ASTM D 2434-68. (2000). *Standard test method for permeability of granular soils (constant head)*. ASTM International, West Conshohocken, PA.
- Atkins, M. (2016). Velocity field measurement using particle image velocimetry (PIV). In *Application of Thermo-Fluidic Measurement Techniques* (pp. 125–166). Elsevier.
- Brevis, W., Niño, Y., & Jirka, G. (2011). Integrating cross-correlation and relaxation algorithms for particle tracking velocimetry. *Experiments in Fluids*, 50(1), 135–147.
- Foster, M., Fell, R., & Spannagle, M. (2000). The statistics of embankment dam failures and accidents. *Canadian Geotechnical Journal*, 37(5), 1000–1024.
- Garcia, X., Akanji, L. T., Blunt, M. J., Matthai, S. K., & Latham, J. P. (2009). Numerical study of the effects of particle shape and polydispersity on permeability. *Physical Review E*, 80(2), 021304. <https://doi.org/10.1103/PhysRevE.80.021304>
- Geuzaine, C., & Remacle, J.-F. (2009). Gmsh: A 3-D finite element mesh generator with built-in pre-and post-processing facilities. *International Journal for Numerical Methods in Engineering*, 79(11), 1309–1331.
- Gollin, D., Brevis, W., Bowman, E. T., & Shepley, P. (2017). Performance of PIV and PTV for granular flow measurements. *Granular Matter*, 19(3), 42.
- Huang, A. Y., Huang, M. Y., Capart, H., & Chen, R.-H. (2008). Optical measurements of pore geometry and fluid velocity in a bed of irregularly packed spheres. *Experiments in Fluids*, 45(2), 309–321.
- Hunter, R. P., & Bowman, E. T. (2018). Visualisation of seepage-induced suffusion and suffusion within internally erodible granular media. *Géotechnique*, 68(10), 918–930. <https://doi.org/10.1680/jgeot.17.P.161>
- ICOLD, C. (2015). Internal erosion of existing dams, levees and dikes, and their foundations. *Bulletin*.
- Iskander, M., Bathurst, R., & Omidvar, M. (2015). Past, present, and future of transparent soils. *Geotechnical Testing Journal*, 38(5), 557–573.
- Karadimitriou, N., & Hassanizadeh, S. (2012). A review of micromodels and their use in two-phase flow studies. *Vadose Zone Journal*, 11(3), vzj2011-0072.
- Karadimitriou, N., Musterd, M., Kleingeld, P., Kreutzer, M., Hassanizadeh, S., & Joekear-Niasar, V. (2013). On the fabrication of PDMS micromodels by rapid prototyping, and their use in two-phase flow studies. *Water Resources Research*, 49(4), 2056–2067.
- Keane, R. D., & Adrian, R. J. (1993). Theory and simulation of particle image velocimetry. *Fifth International Conference on Laser Anemometry: Advances and Applications*, 2052, 477–492.

676 Khalili, A., Basu, A., & Pietrzyk, U. (1998). Flow visualization in porous media via positron
677 emission tomography. *Physics of Fluids*, 10(4), 1031–1033.

678 Knight, C., O’Sullivan, C., van Wachem, B., & Dini, D. (2020). Computing drag and interactions
679 between fluid and polydisperse particles in saturated granular materials. *Computers and*
680 *Geotechnics*, 117, 103210. <https://doi.org/10.1016/j.compgeo.2019.103210>

681 Lorensen, W. E., & Cline, H. E. (1987). Marching cubes: A high resolution 3D surface
682 construction algorithm. *ACM Siggraph Computer Graphics*, 21(4), 163–169.

683 Meinhart, C. D., Wereley, S. T., & Santiago, J. G. (1999). PIV measurements of a microchannel
684 flow. *Experiments in Fluids*, 27(5), 414–419.

685 Michaelis, D., Neal, D. R., & Wieneke, B. (2016). Peak-locking reduction for particle image
686 velocimetry. *Measurement Science and Technology*, 27(10), 104005.

687 Mostaghimi, P., Blunt, M. J., & Bijeljic, B. (2013). Computations of absolute permeability on
688 micro-CT images. *Mathematical Geosciences*, 45(1), 103–125.

689 Muir Wood, D. (2007). The magic of sands—The 20th Bjerrum Lecture presented in Oslo, 25
690 November 2005. *Canadian Geotechnical Journal*, 44(11), 1329–1350.

691 Northrup, M. A., Kulp, T. J., Angel, S. M., & Pinder, G. F. (1993). Direct measurement of
692 interstitial velocity field variations in a porous medium using fluorescent-particle image
693 velocimetry. *Chemical Engineering Science*, 48(1), 13–21.

694 Nunes, J. P., Bijeljic, B., & Blunt, M. (2015). Time-of-flight distributions and breakthrough
695 curves in heterogeneous porous media using a pore-scale streamline tracing algorithm.
696 *Transport in Porous Media*, 109(2), 317–336.

697 OpenFOAM Foundation. (2019). *OpenFOAM v7 User Guide*. [https://cfd.direct/openfoam/user-](https://cfd.direct/openfoam/user-guide)
698 [guide](https://cfd.direct/openfoam/user-guide)

699 Otsu, N. (1979). A threshold selection method from gray-level histograms. *IEEE Transactions*
700 *on Systems, Man, and Cybernetics*, 9(1), 62–66.

701 Patil, V. A., & Liburdy, J. A. (2013). Flow characterization using PIV measurements in a low
702 aspect ratio randomly packed porous bed. *Experiments in Fluids*, 54(4), 1497.

703 Peurrung, L. M., Rashidi, M., & Kulp, T. J. (1995). Measurement of porous medium velocity
704 fields and their volumetric averaging characteristics using particle tracking velocimetry.
705 *Chemical Engineering Science*, 50(14), 2243–2253.

706 Piller, M., Casagrande, D., Schena, G., & Santini, M. (2014). Pore-scale simulation of laminar
707 flow through porous media. *Journal of Physics: Conference Series*, 501(1), 012010.

708 Preene, M., & Rosser, M. (2012). *Groundwater lowering in construction: A practical guide to*
709 *dewatering* (Vol. 6). CRC Press.

710 Rong, L. W., Dong, K. J., & Yu, A. B. (2013). Lattice-Boltzmann simulation of fluid flow
711 through packed beds of uniform spheres: Effect of porosity. *Chemical Engineering*
712 *Science*, 99, 44–58. <https://doi.org/10.1016/j.ces.2013.05.036>

- Ronneberger, O., Fischer, P., & Brox, T. (2015). U-net: Convolutional networks for biomedical image segmentation. *International Conference on Medical Image Computing and Computer-Assisted Intervention*, 234–241.
- Saleh, S., Thovert, J., & Adler, P. (1992). Measurement of two-dimensional velocity fields in porous media by particle image displacement velocimetry. *Experiments in Fluids*, 12(3), 210–212.
- Sanvitale, N., & Bowman, E. T. (2012). Internal imaging of saturated granular free-surface flows. *International Journal of Physical Modelling in Geotechnics*, 12(4), 129–142.
- Schindelin, J., Arganda-Carreras, I., Frise, E., Kaynig, V., Longair, M., Pietzsch, T., Preibisch, S., Rueden, C., Saalfeld, S., Schmid, B., & others. (2012). Fiji: An open-source platform for biological-image analysis. *Nature Methods*, 9(7), 676–682.
- Sederman, A., Johns, M., Bramley, A., Alexander, P., & Gladden, L. (1997). Magnetic resonance imaging of liquid flow and pore structure within packed beds. *Chemical Engineering Science*, 52(14), 2239–2250.
- Soille, P. (2013). *Morphological image analysis: Principles and applications*. Springer Science & Business Media.
- Taylor, H., O’sullivan, C., & Sim, W. (2016). Geometric and hydraulic void constrictions in granular media. *Journal of Geotechnical and Geoenvironmental Engineering*, 142(11), 04016057.
- Taylor, H., O’Sullivan, C., Sim, W. W., & Carr, S. J. (2017). Sub-particle-scale investigation of seepage in sands. *Soils and Foundations*, 57(3), 439–452.
- Thaker, A. H., Karthik, G., & Buwa, V. V. (2019). PIV measurements and CFD simulations of the particle-scale flow distribution in a packed bed. *Chemical Engineering Journal*, 374, 189–200.
- Thielicke, W. (2014). *The flapping flight of birds: Analysis and application* [PhD Thesis]. University of Groningen.
- Thielicke, W., & Stamhuis, E. (2014). PIVlab—towards user-friendly, affordable and accurate digital particle image velocimetry in MATLAB. *Journal of Open Research Software*, 2(1).
- Vogt, N., Simpson, B., Van Seters, A., Gens, A., Odenwald, B., Moller, H., Habert, J., & Panu, T. (2015). TC250/SC7/EG9: Water pressures. *Final Report: Proposal of Changes to EC7-1*.
- Wiederseiner, S., Andreini, N., Epely-Chauvin, G., & Ancey, C. (2011). Refractive-index and density matching in concentrated particle suspensions: A review. *Experiments in Fluids*, 50(5), 1183–1206.
- Zhang, L., & Chen, Q. (2006). Seepage failure mechanism of the Gouhou rockfill dam during reservoir water infiltration. *Soils and Foundations*, 46(5), 557–568.
- Zhao, B., Wang, J., Coop, M., Viggiani, G., & Jiang, M. (2015). An investigation of single sand particle fracture using X-ray micro-tomography. *Géotechnique*, 65(8), 625–641.

752 Zick, A. A., & Homsy, G. M. (1982). Stokes flow through periodic arrays of spheres. *Journal of*
753 *Fluid Mechanics*, 115(1), 13. <https://doi.org/10.1017/S0022112082000627>
754
755

Table 1. Particle and fluid properties

	Particle diameter [mm]	Density [g/cm ³]	Refractive index	Viscosity	
				Kinematic [mm ² /s]	Dynamic [Pa·s]
SiLibeads Glass beads Type P Borosilicate	7.5 ± 0.03	2.23	1.46 (*)	-	
Duran® angular particles	6.7 – 9.5	2.23	1.47 (at 21°C)	-	
Cargille immersion fluid	-	0.846	1.47 (at 25°C)	16 (at 25 °C)	0.0135
Microsphere fluid seeding particles	0.005 – 0.030	0.750	-	-	

(*) The measurement temperature for the refractive index value was not given on the material certificate. A sensitivity analysis to temperature was conducted to achieve the optimum optical transparency with the immersion fluid.

Table 2. Sub-volume dimensions

Sub-volume	Dimensions, x × y × z [mm ³]
Beads-U	37.4 × 23.4 × 25
Beads-L	40.4 × 25.3 × 25
Ang-U	38.5 × 24.0 × 25
Ang-L	38.5 × 24.0 × 25

768

769 Table 3. Experimental and numerical measurements for each sub-volume

Sub-volume	n	i_{Exp}	A_{Exp} [cm ²]	Q_{Exp} [ml/s]	u_{seep}^{Exp} [mm/s]	u_{seep}^{PIV} [mm/s]	u_{seep}^{CFD} [mm/s]
Beads-U	0.38	0.086	100	30.3	8.0	7.1	6.8
Beads-L	0.38	0.086	100	30.3	8.0	5.7	6.2
Ang-U	0.36	0.143	100	28.5	7.9	4.5	6.0
Ang-L	0.36	0.114	100	28.5	7.9	4.5	5.9

770

Figure 1. Schematic of the experimental set up.

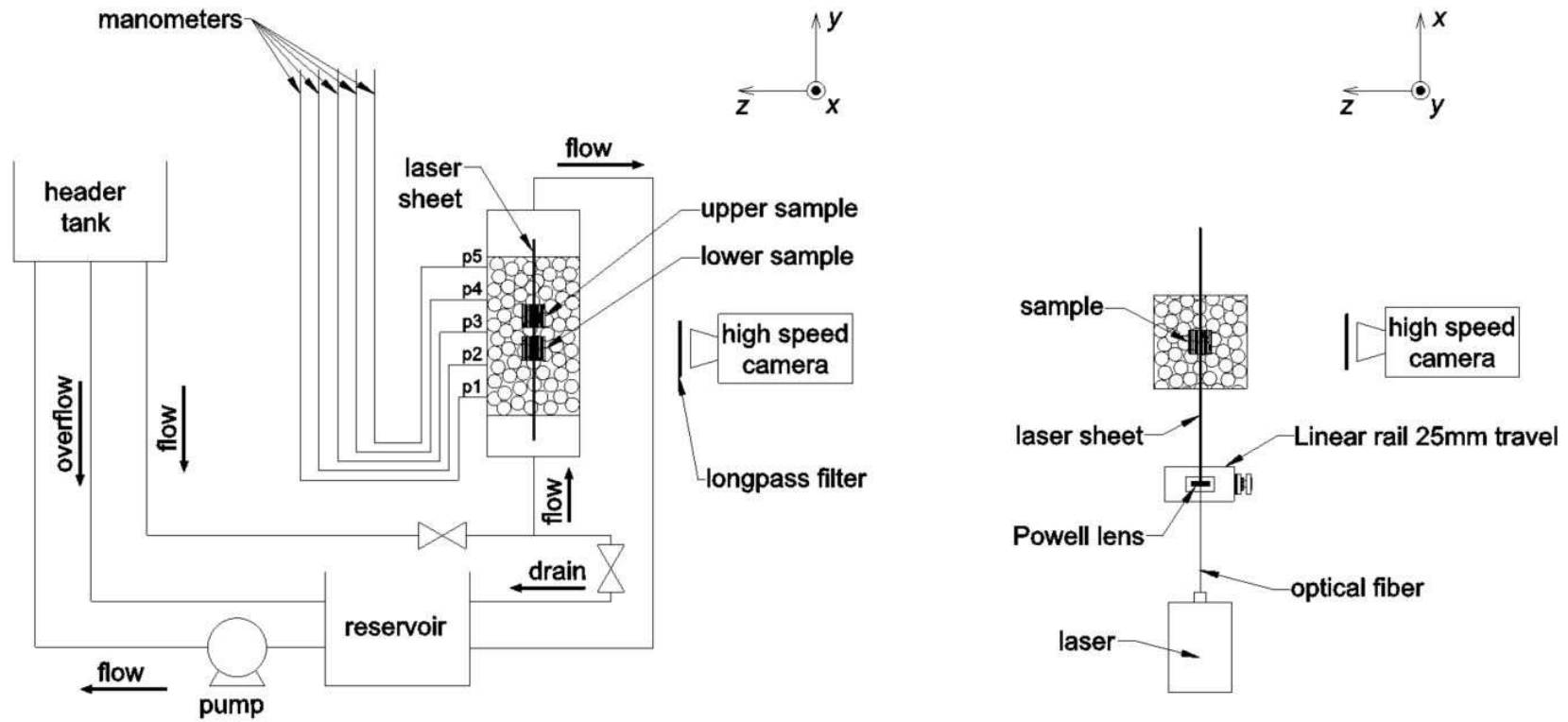


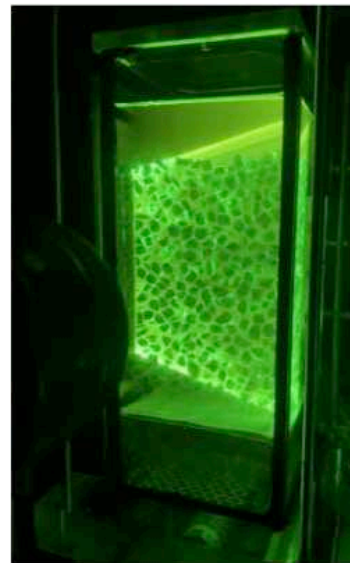
Figure 2. Images of experimental setup: (a) Permeameter cell partially filled with oil; (b) Beads sample illuminated by laser sheet; (c) Angular particles sample illuminated by laser sheet; (d) top view of the laser sheet.



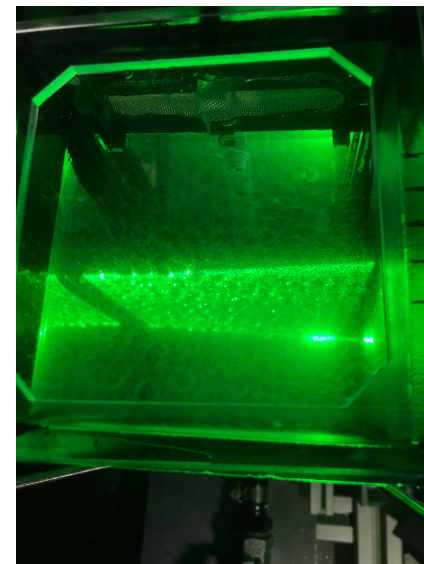
(a)



(b)



(c)



(d)

Figure 3. Flow fields in the (a) left, (b) middle and (c) right for the permeameter with beads.

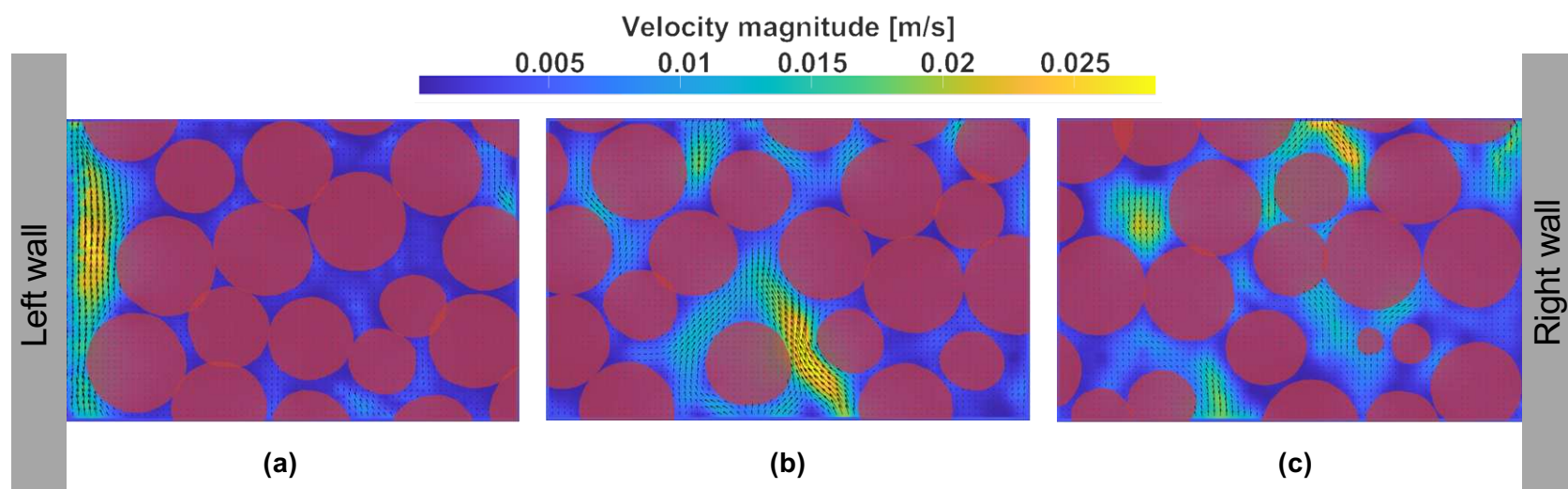


Figure 4. (a) Typical grey-scale image in Beads-U sub-volume, $z = 0$ mm. (b) Histogram of grey values. Inset in (a) shows that the non-uniform intensity is a consequence of the finite laser width.

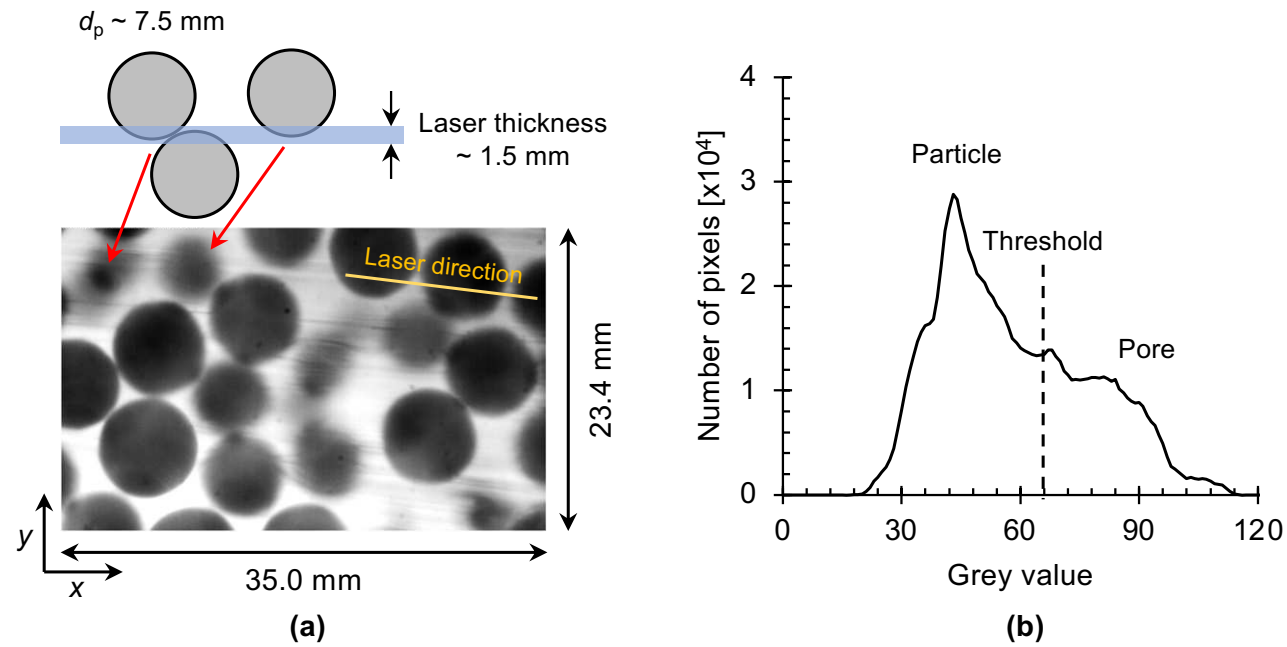


Figure 5. Segmentation results for three typical slices in Beads-U sub-volume using three different segmentation methods: threshold segmentation with Otsu's threshold, trainable Weka segmentation, and U-Net segmentation. Note: dashed circles indicate the artifacts produced by inaccurate segmentation.

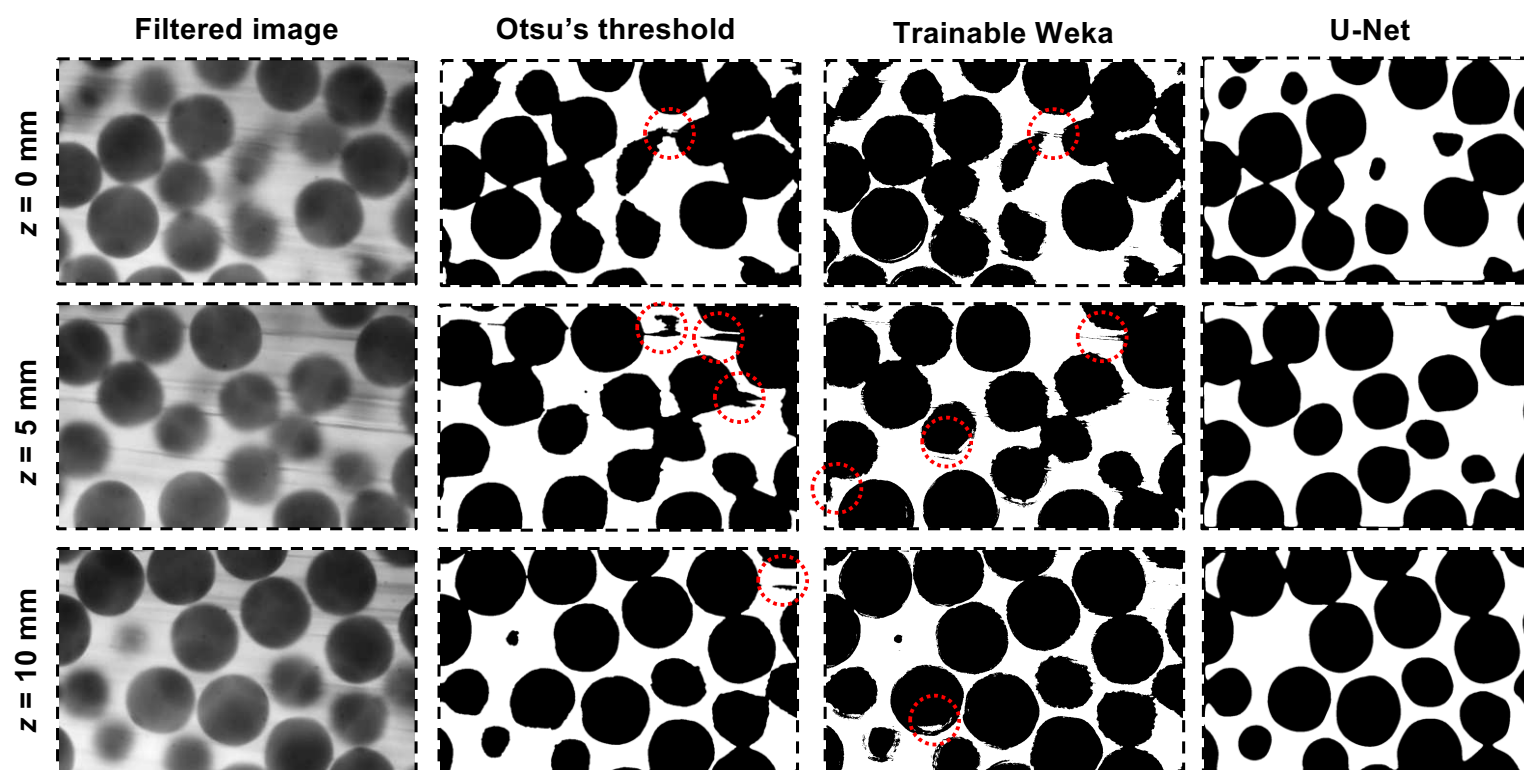


Figure 6. U-Net segmentation procedure for Beads-U sub-volume: (a) Step-1: prepare training and validating data sets; (b) Step-2: train U-Net algorithm; (c) Step-3: apply trained U-Net as a classifier for segmenting new images.

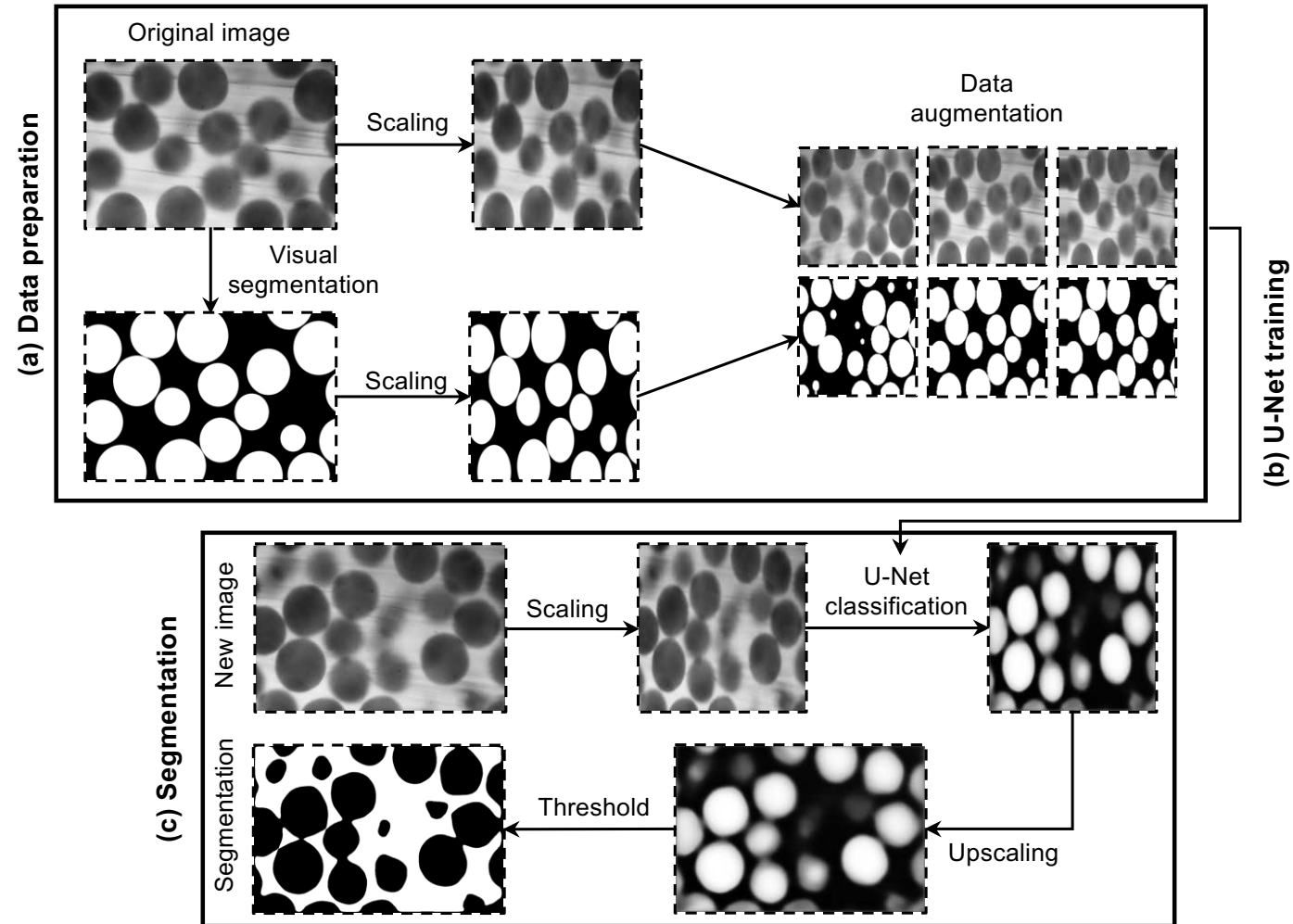


Figure 7. Upscaling along z-direction on the U-Net classified image for Beads-U sub-volume: (a) Unscaled image data; (b) Image obtained by scaling without interpolation; (c) Image obtained by scaling with bilinear interpolation; (d) Image obtained by scaling with bicubic interpolation.

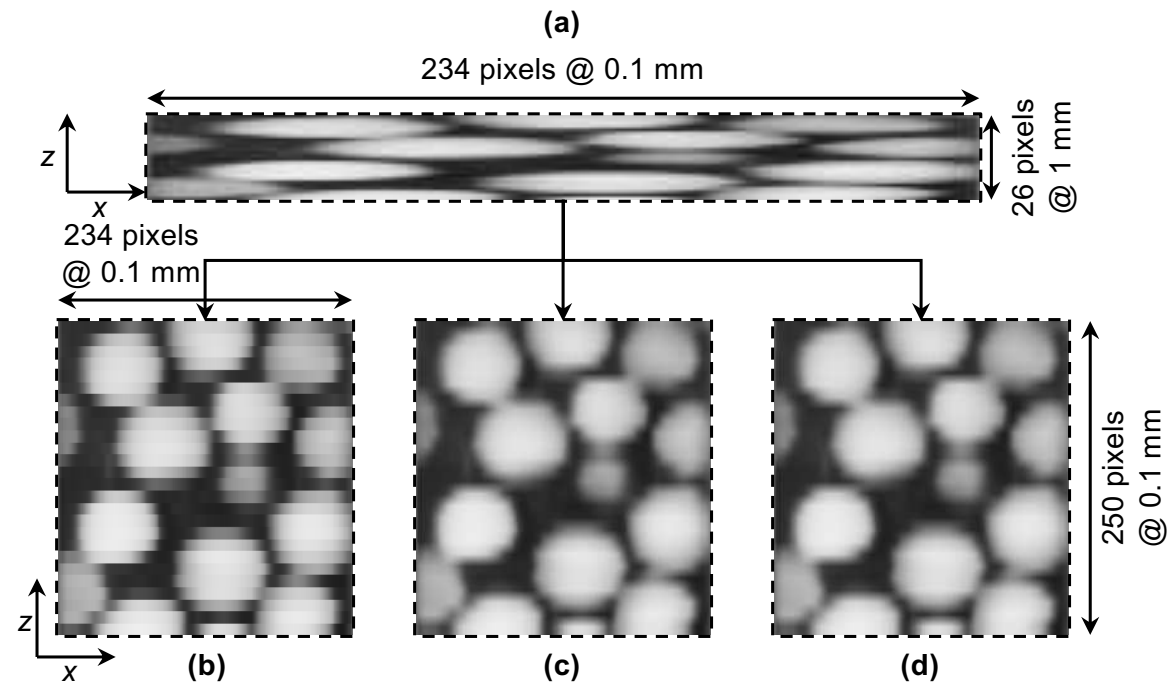


Figure 8. Labelled images with particles represented by different colours for Beads-U sub-volume on (a) x-y plane and (b) x-z plane and Ang-U sub-volume on (c) x-y plane and (d) x-z plane.

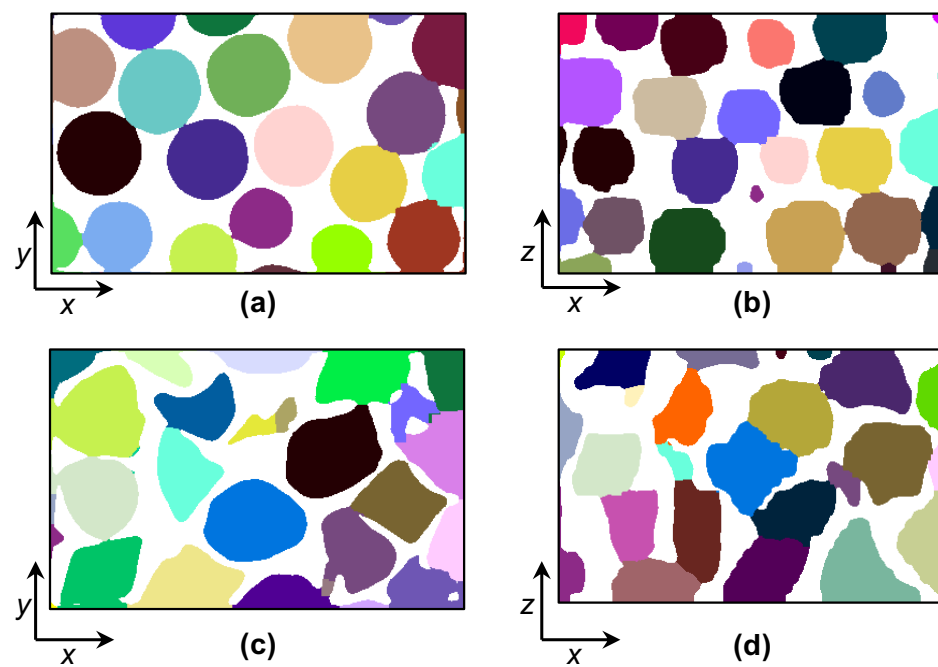


Figure 9. Three-dimensional views of the combined surface meshes for (a) Beads-U sub-volume and (b) Ang-U sub-volume. Note: colour is used to distinguish the surfaces of individual particles. Hexahedron meshes which discretize pore structure for CFD simulation for (c) Beads-U sub-volume and (d) Ang-U sub-volume.

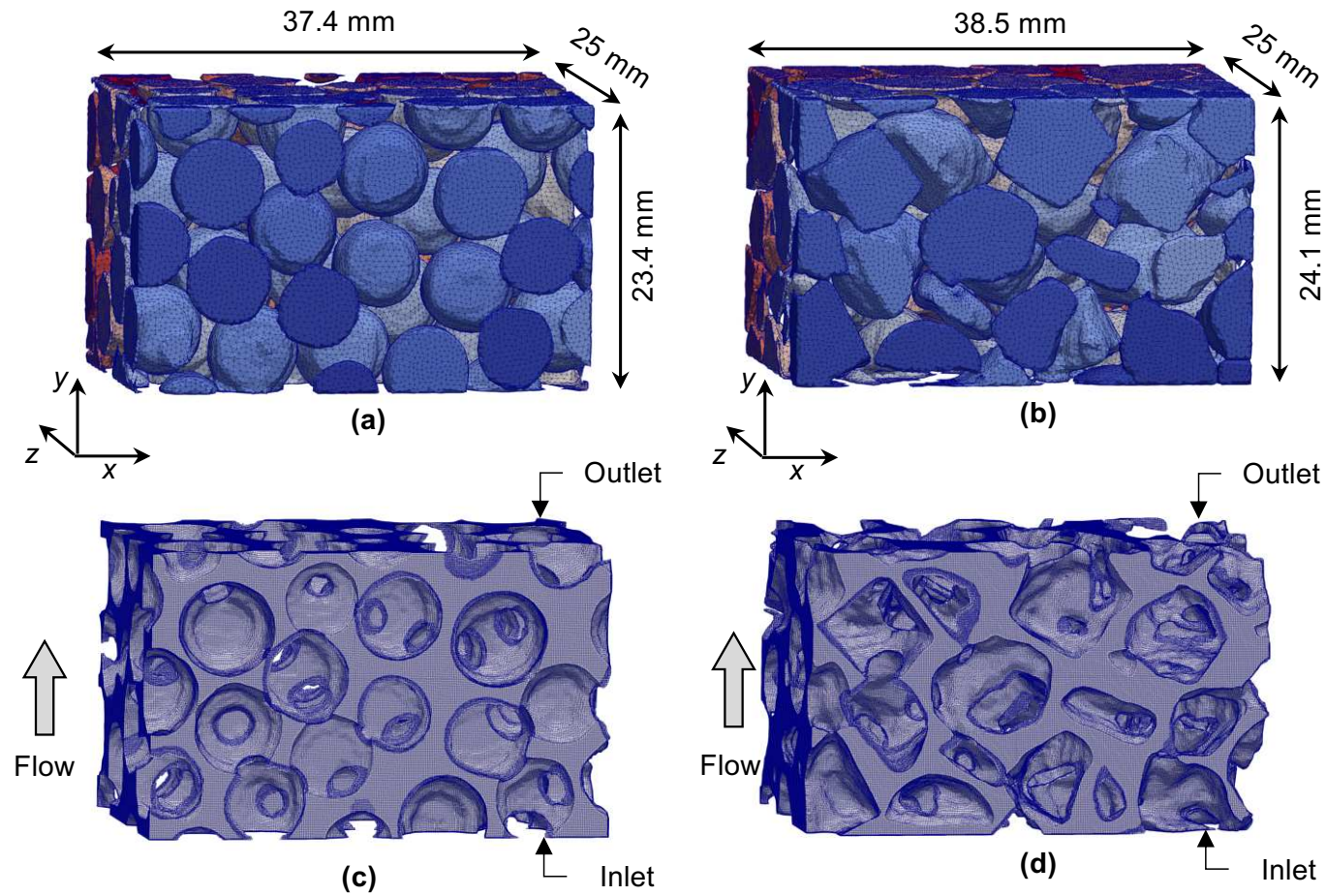


Figure 10. Verification of CFD modelling approach: (a) Confirmation of ability to capture the influence of porosity on the fluid-particle interaction coefficient $\bar{F}_{f \rightarrow s}$, dashed lines indicate a curve fit to the Zick & Homsy (1982) data; (b) Mesh dependence of $\bar{F}_{f \rightarrow s}$ for SC packings; (c) Mesh dependence of $\bar{F}_{f \rightarrow s}$ for FCC packings. The results predicted by the Immersed Boundary Method (IBM) with a regular grid and from fully resolved CFD using an unstructured meshes from Knight et al. (2020) are included in (a) and (c), respectively.

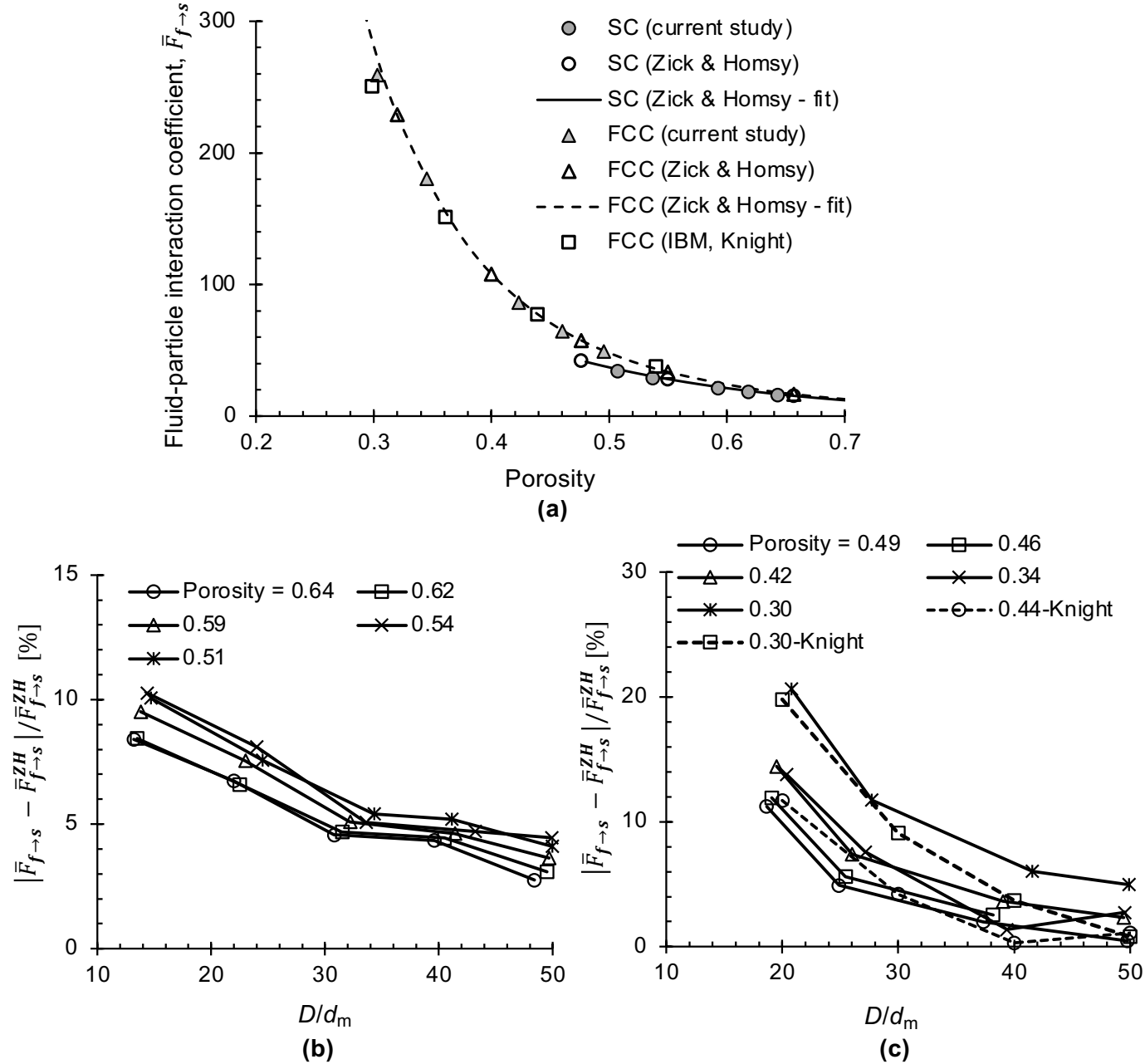


Figure 11. (a) Hydraulic permeability values predicted by experiments, PIV and CFD measurements. (b) Influence of porosity on hydraulic permeability as estimated by CFD modelling for Beads-U and Ang-U sub-volumes. The prediction results from Kozeny-Carman Equation (KC Eq.) is included in (b).

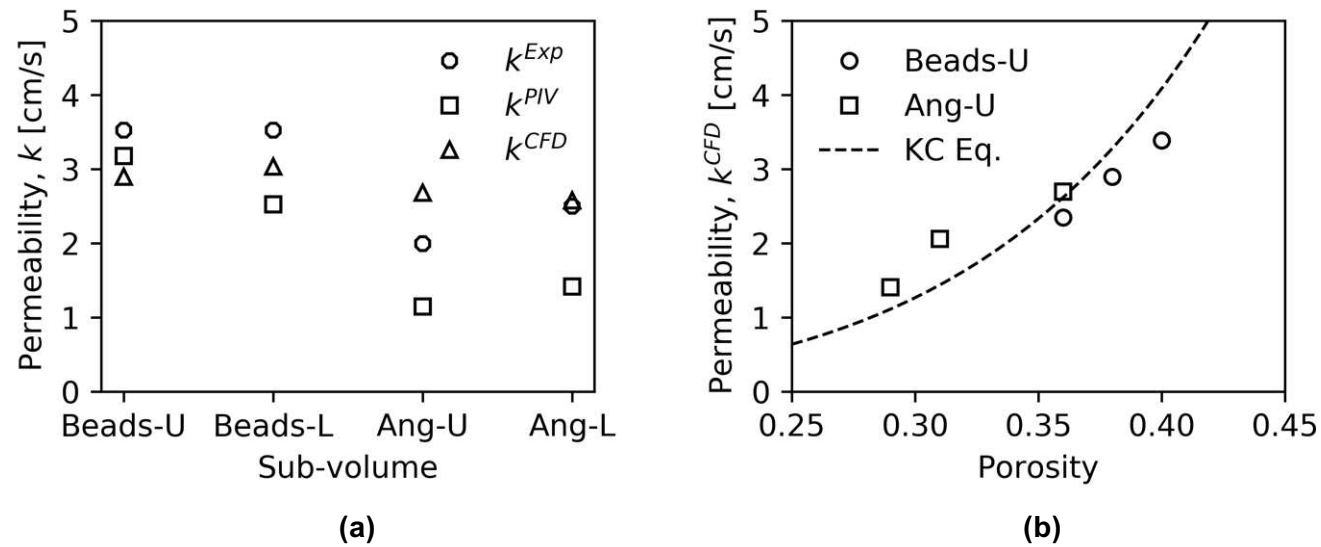


Figure 12. Comparison of the PIV and CFD flow fields in Beads-U sub-volume on the vertical slice with $z = 16$ mm.

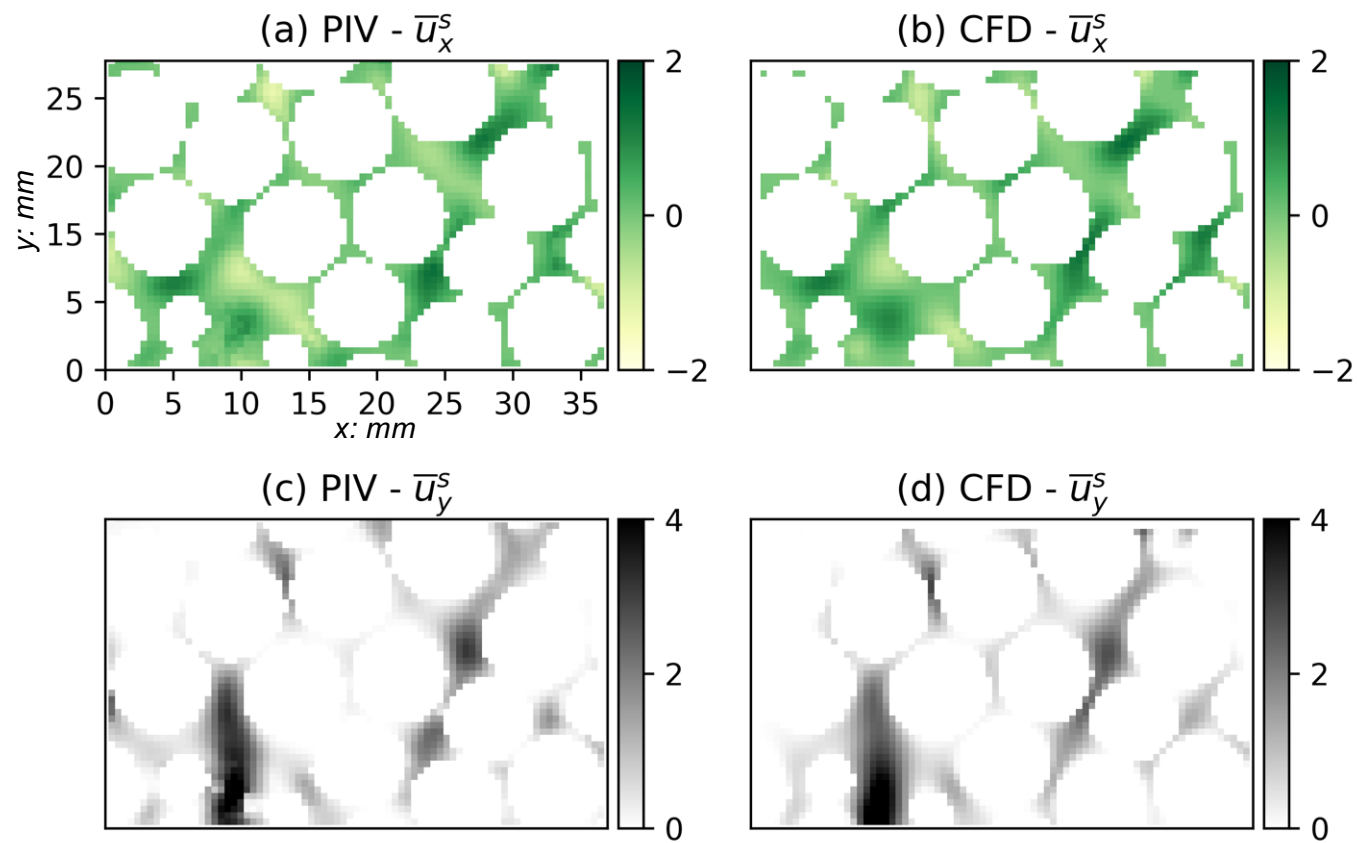


Figure 13. Comparison of the PIV and CFD flow fields in Beads-U sub-volume on three slices with $z = 1, 8$ and 16 mm. Velocity vector length is normalized by seepage velocity.

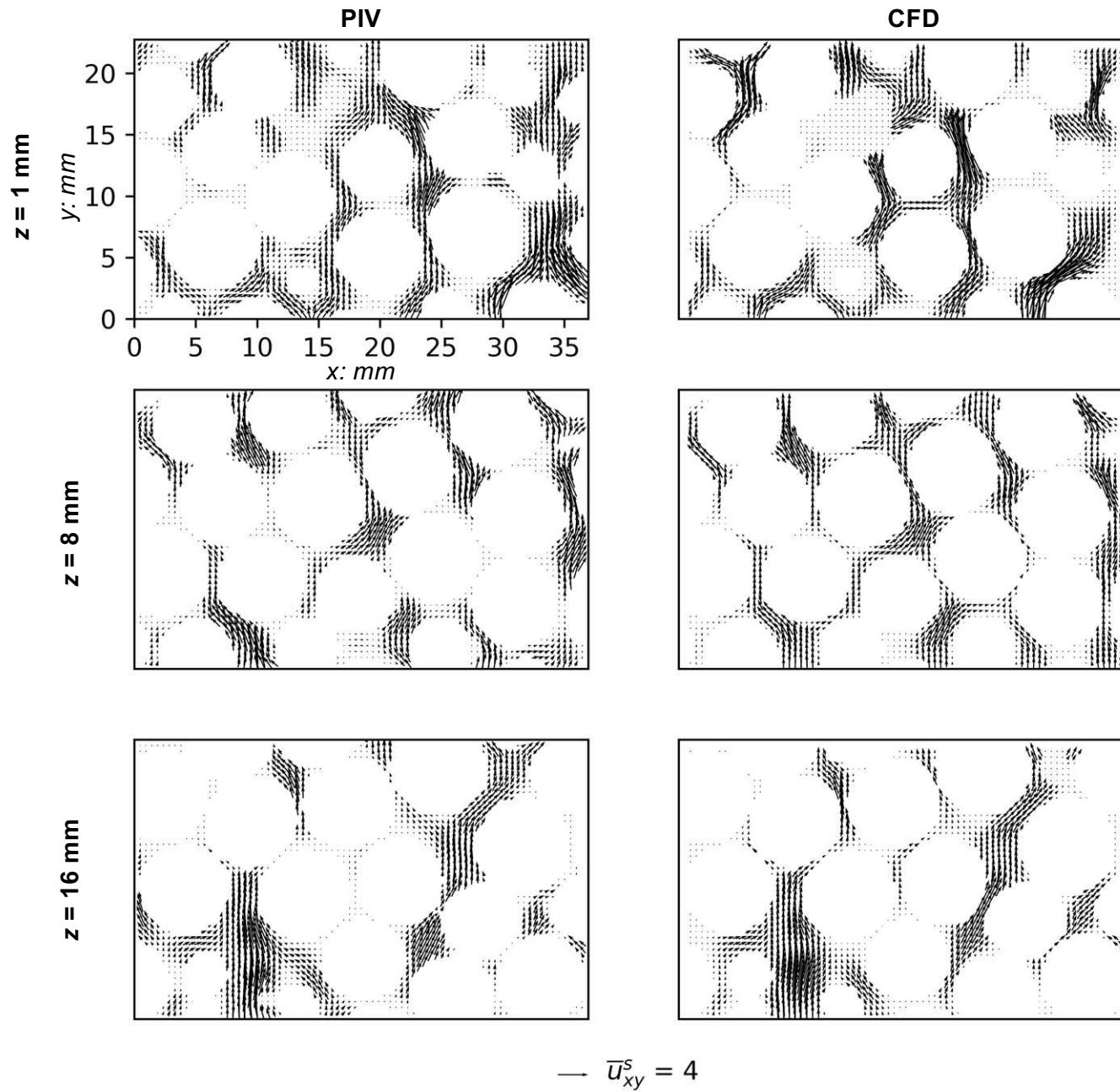


Figure 14. Cumulative distributions of flow velocity at four vertical planes in Beads-U sub-volume obtained from PIV and CFD results.

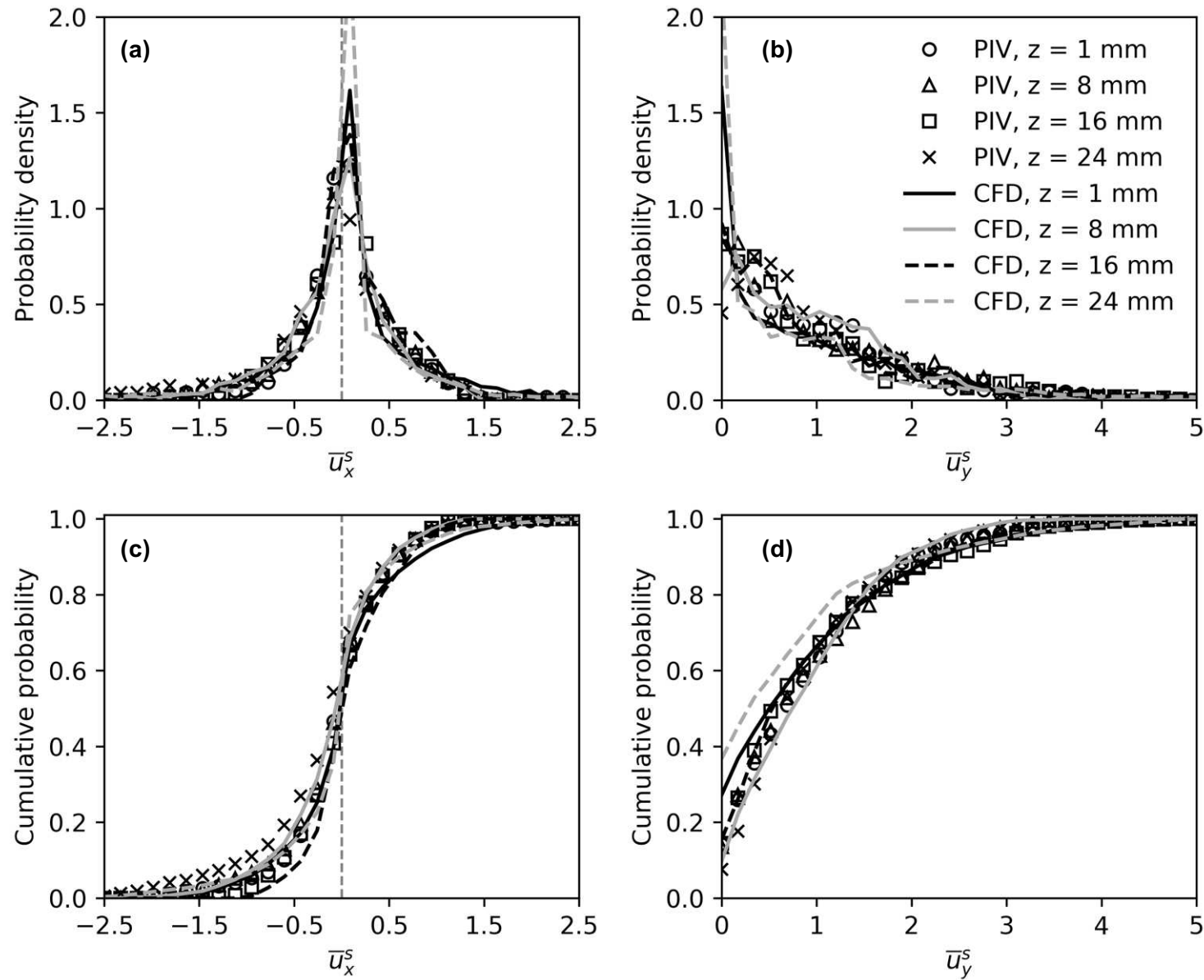


Figure 15. Comparison of the PIV and CFD flow fields in Ang-L sub-volume on three slices with $z = 1, 8$ and 16 mm. Velocity vector length is normalized by seepage velocity. Arrows indicate narrow flow paths.

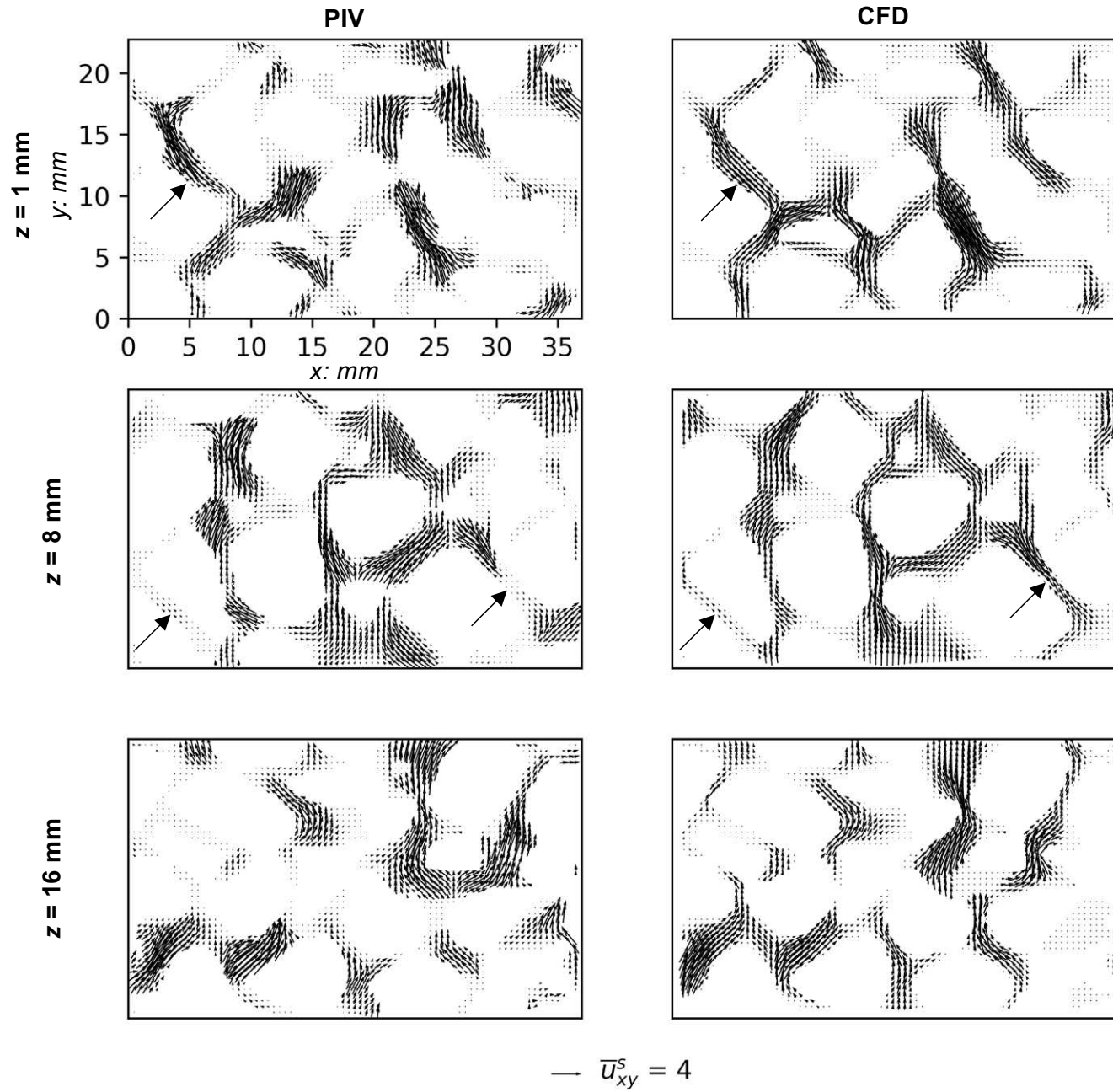


Figure 16. Cumulative distributions of flow velocity at four vertical planes in Ang-L sub-volume obtained from PIV and CFD results.

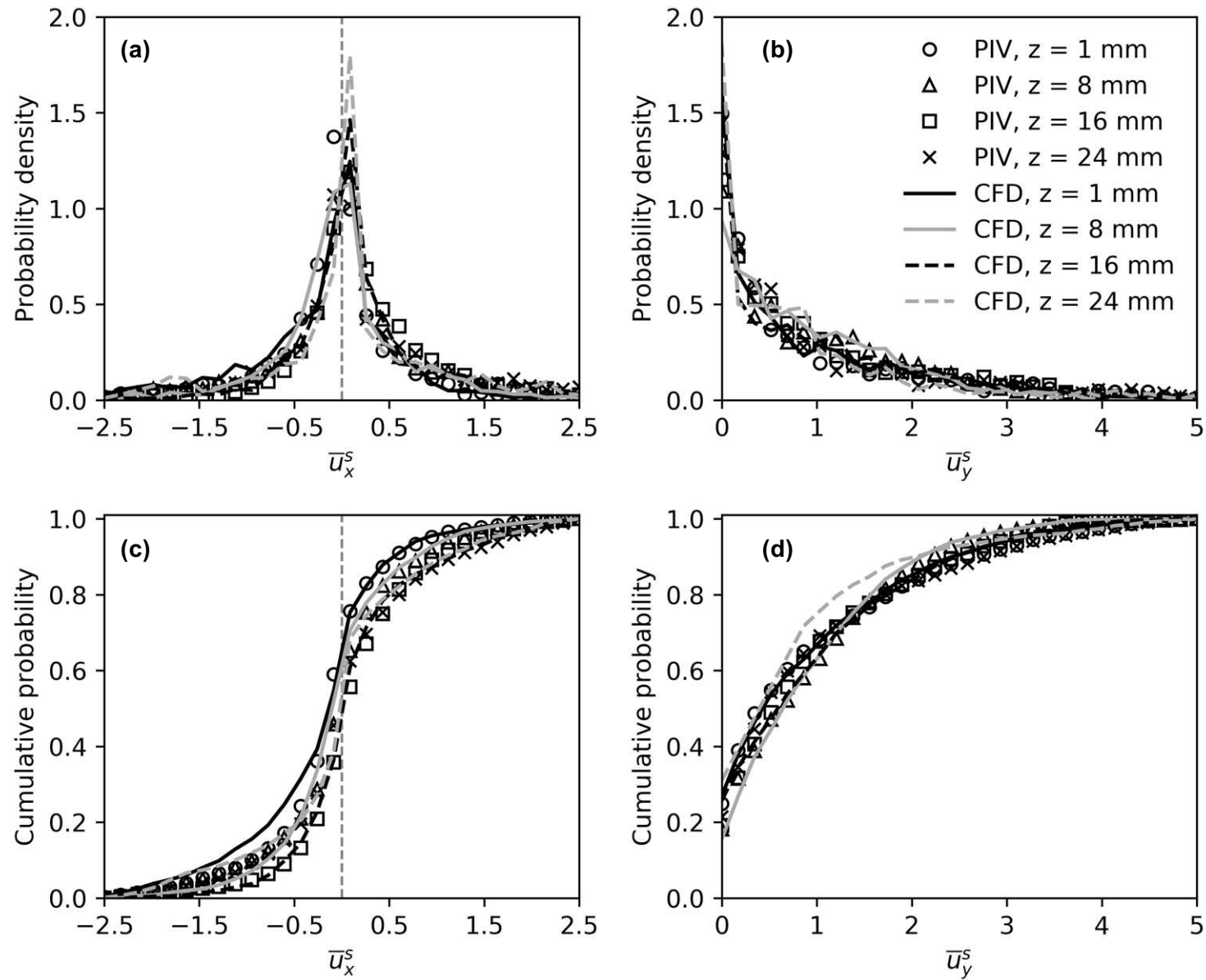


Figure 17. Difference between PIV and CFD flow fields for the vertical slice with $z = 16$ mm in Beads-U sub-volume: (a) horizontal velocity; (b) vertical velocity. The cumulative distributions of PIV and CFD difference for (c) horizontal velocity and (d) vertical velocity on five typical slices in Beads-U sub-volume.

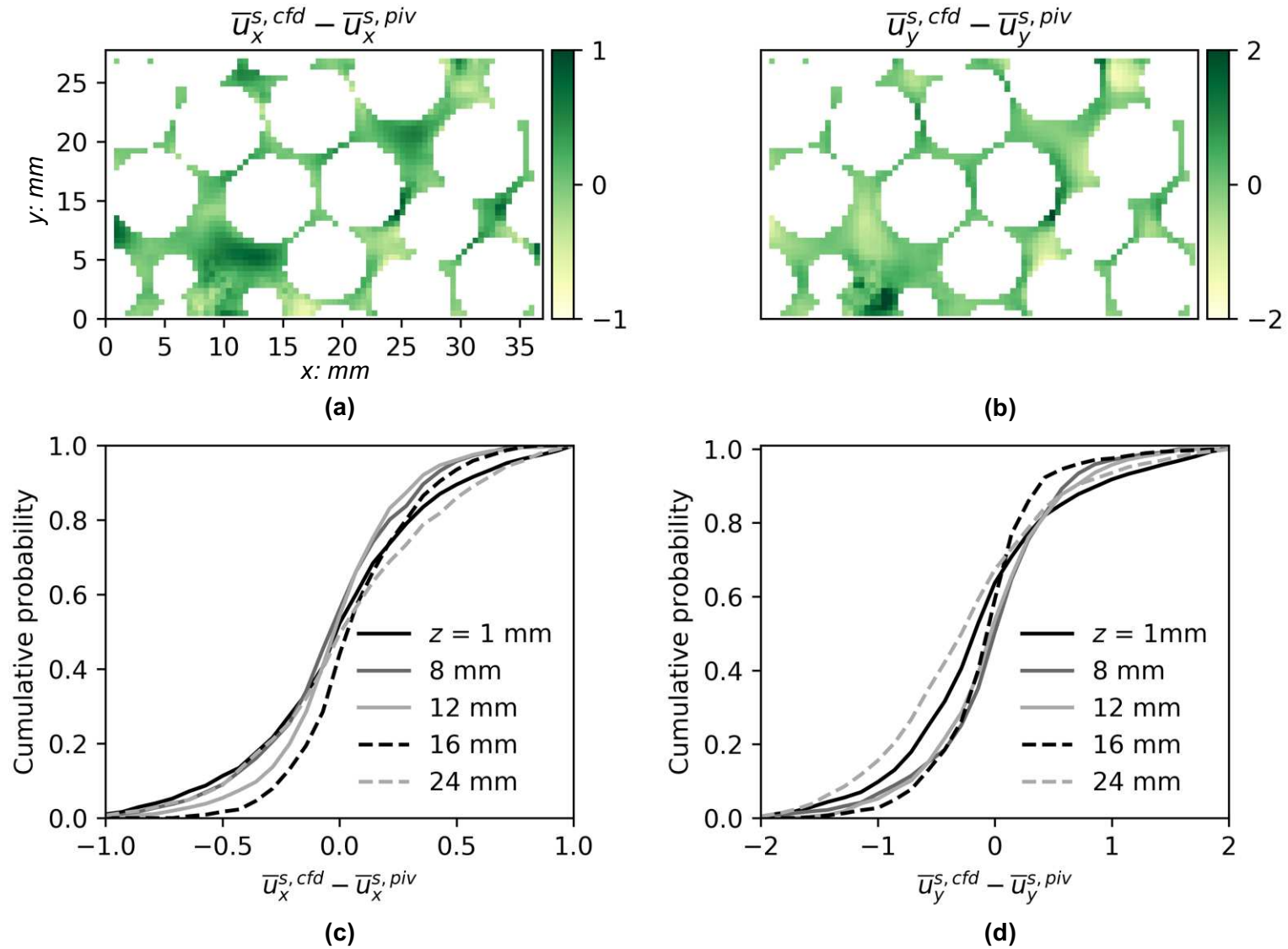


Figure 18. Variation of the mean velocity values obtained from PIV and CFD results and the slice porosity on x-y planes parallel to flow direction.

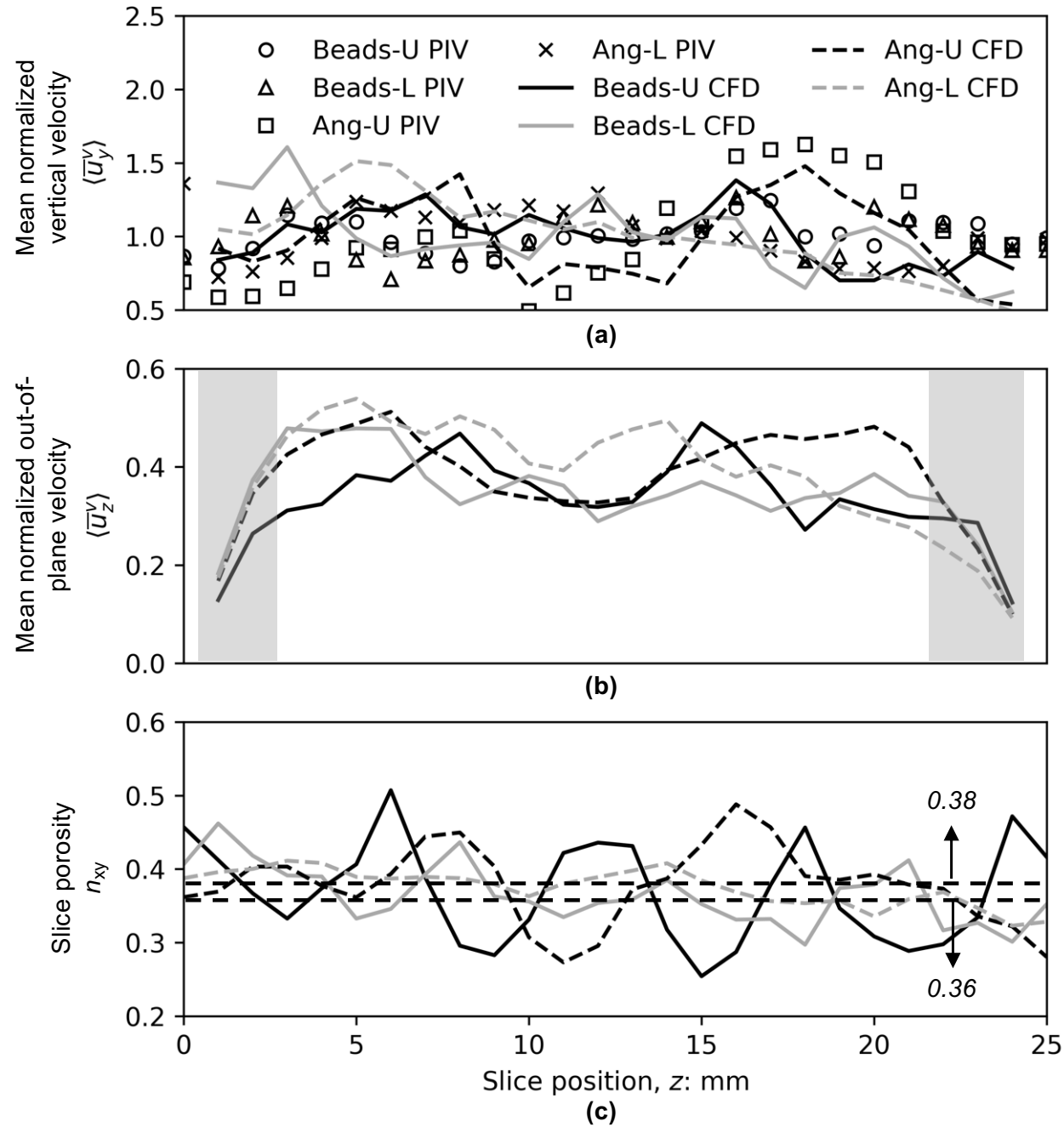


Figure 19. Variation of mean vertical velocity, porosity and hydraulic gradient on x-z planes perpendicular to flow direction predicted by CFD simulations.

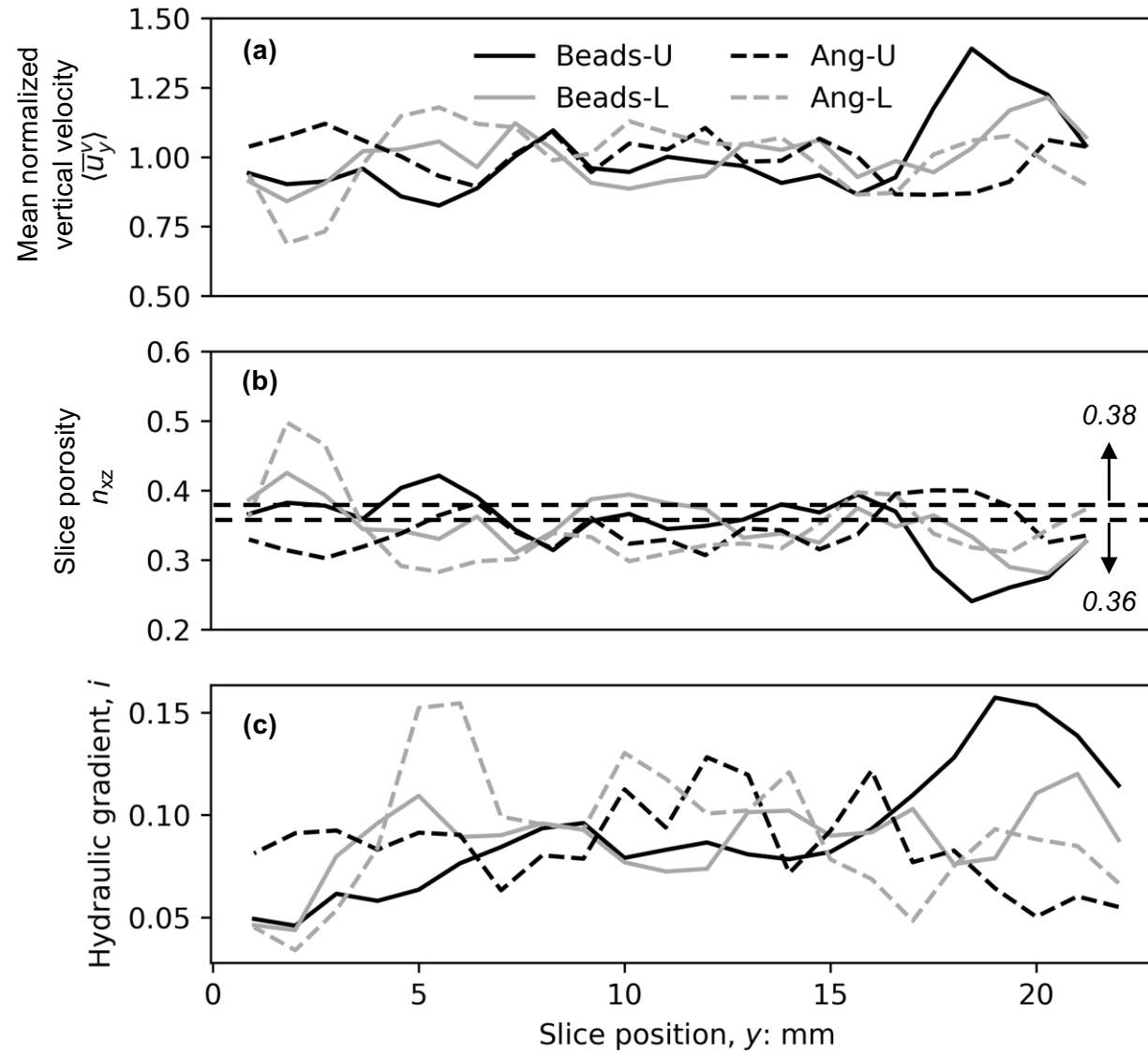


Figure 20. Projection views of drag force vectors for the particles that are not intersecting with boundary walls.

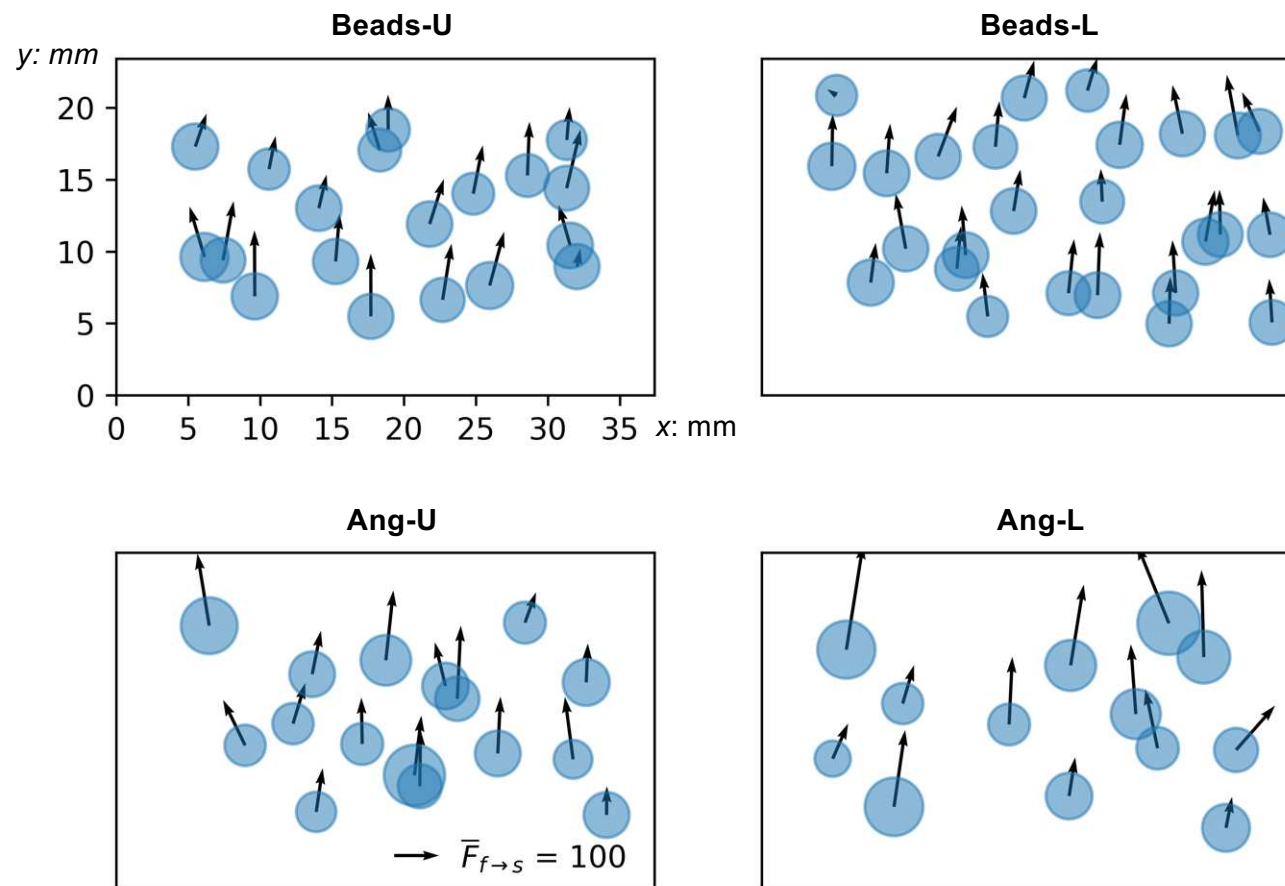


Figure 21. Cumulative distributions of (a) fluid-particle interaction coefficients for beads and angular particles and (b) the normalized fluid-particle interaction coefficients.

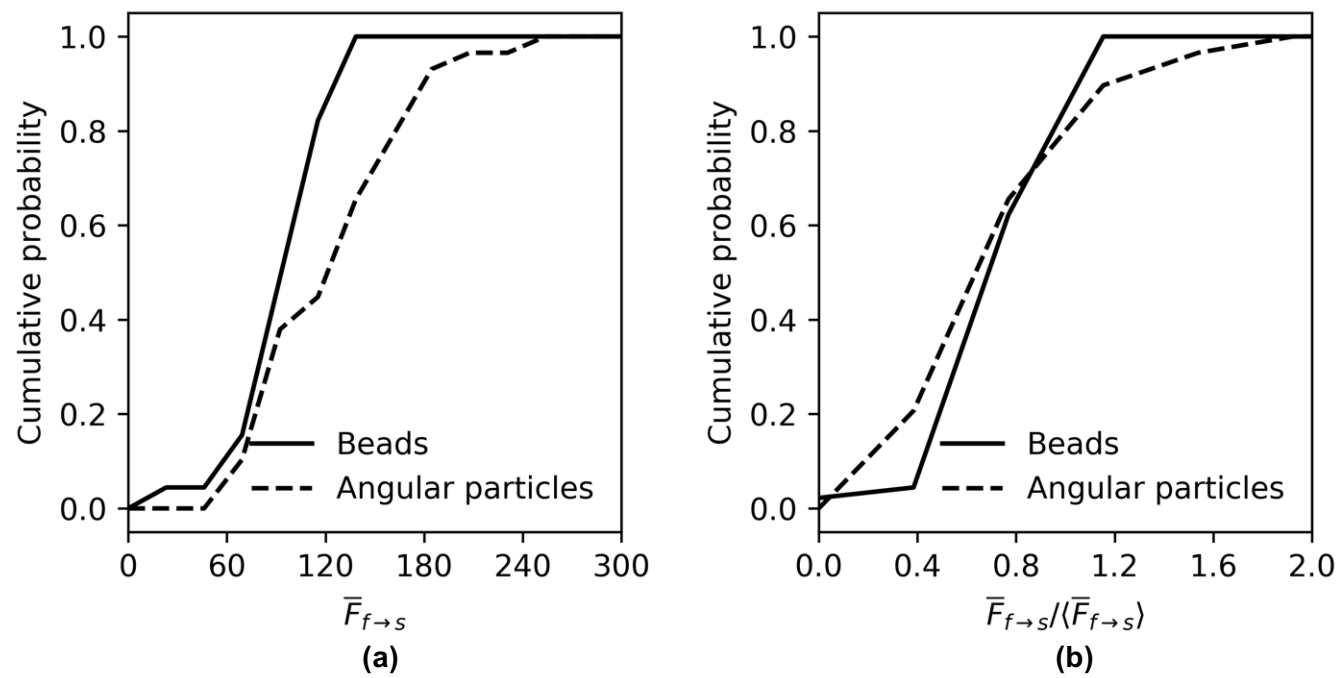


Figure 22. Distributions of (a) the ratio between pressure and viscous drag components, and (b) the angle between fluid-particle interaction and flow direction.

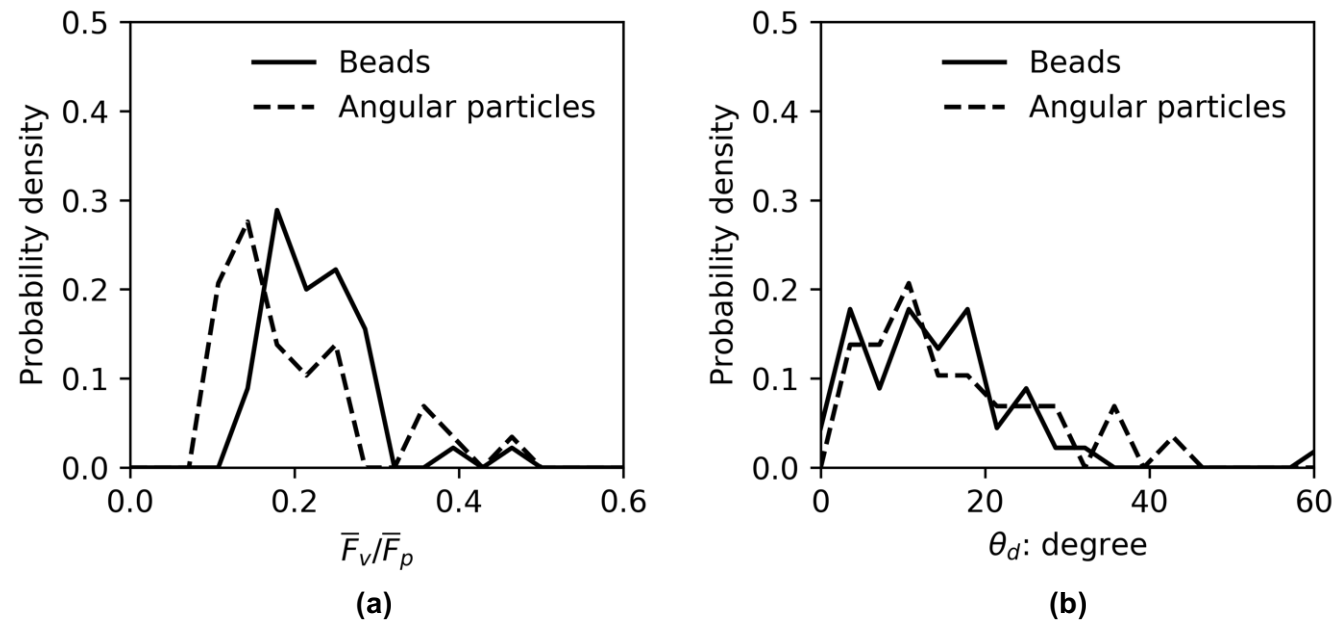


Figure S1. Example of the effect of time resolution of PIV analysis on the estimate of the time averaged component (a) u_x and (b) u_y . The velocities are estimated along the yellow dashed lined shown in the inset of (a).

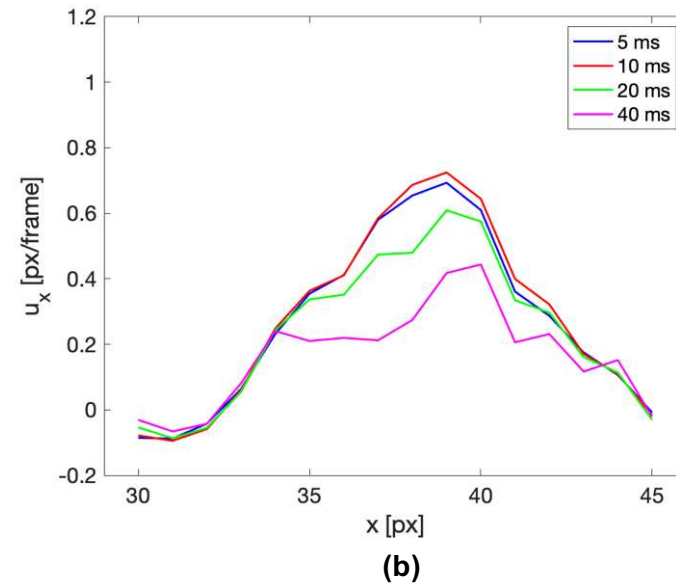
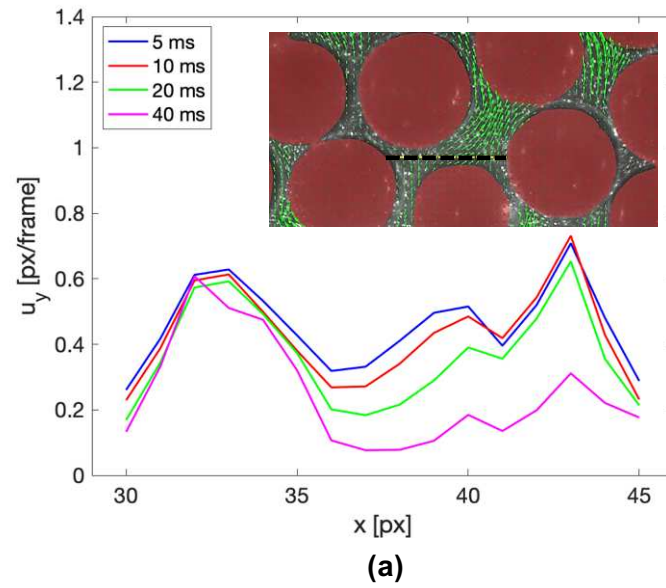
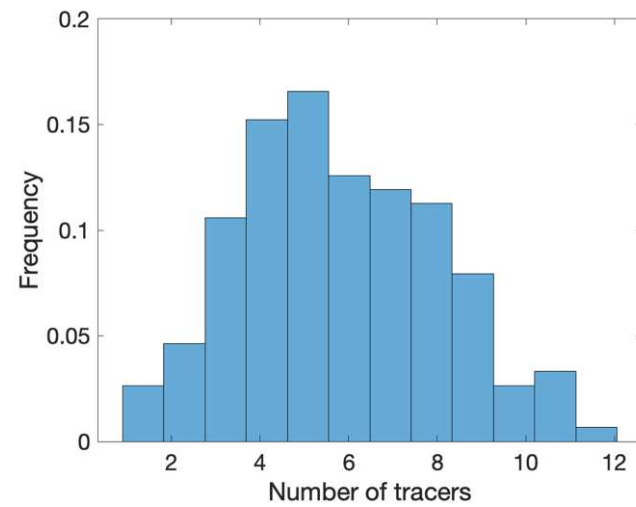
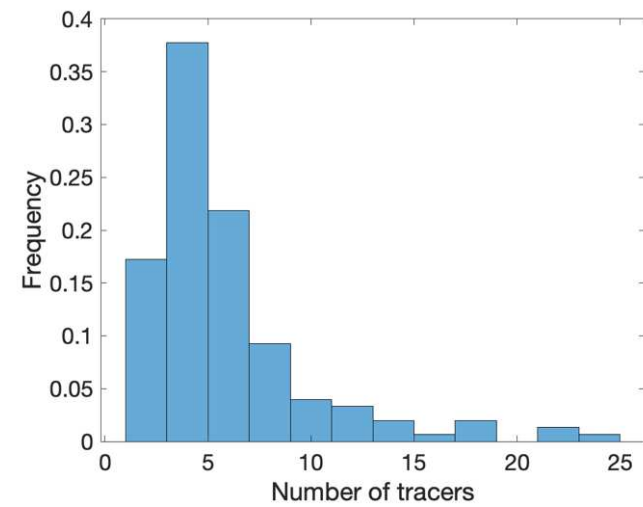


Figure S2. Distribution of the number of tracers for a subsets of interrogation windows (32 x 32 pixels) for (a) beads and (b) angular particles.

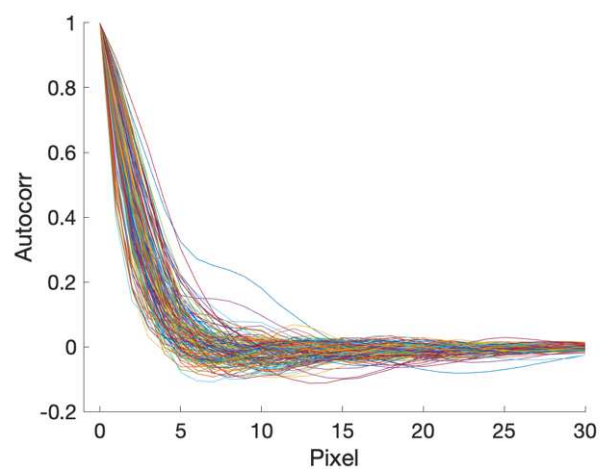


(a)

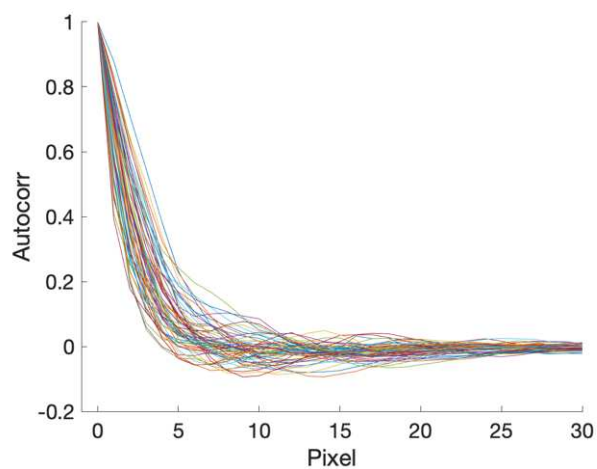


(b)

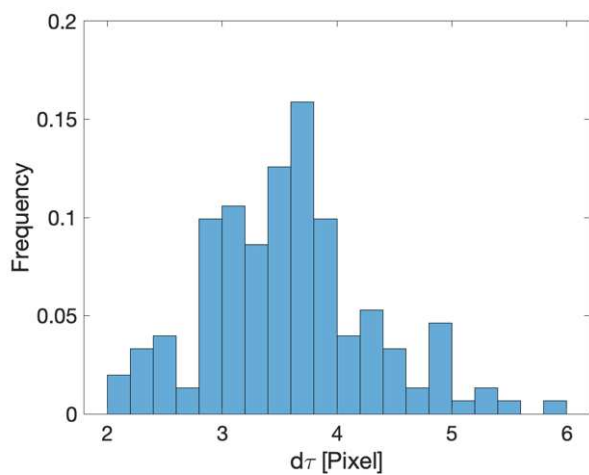
Figure S3. Autocorrelation function for a subsets of interrogation windows (32 x 32 pixels) for (a) beads and (b) angular particles. Histogram of autocorrelation peak width for (c) beads and (d) angular particles.



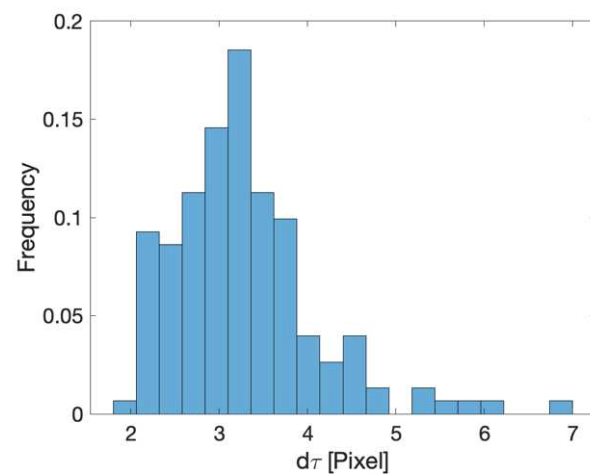
(a)



(b)

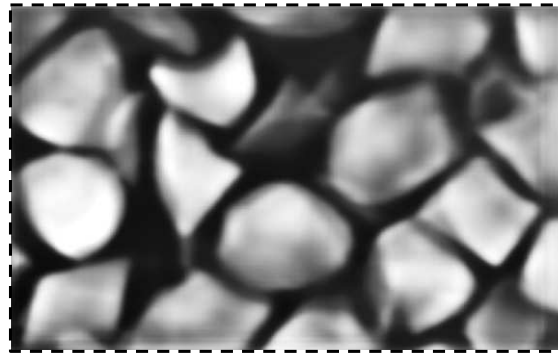


(c)

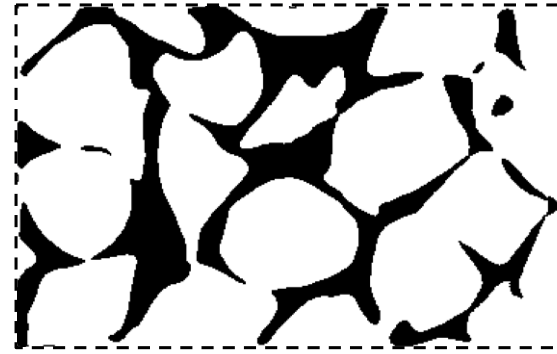


(d)

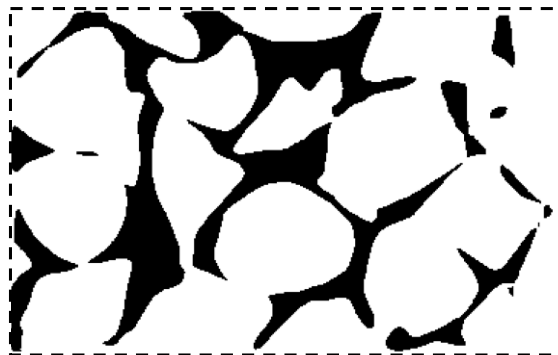
Figure S4. (a) Typical slice of Ang-U processed by U-Net, and the binarization results at different porosity values (b) 0.31, (c) 0.29, and (d) 0.27.



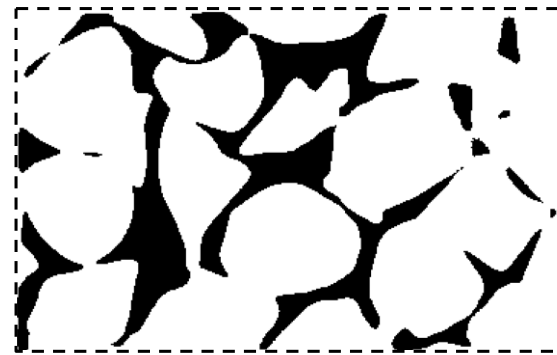
(a)



(b)



(c)



(d)